

Phase-field modeling of fatigue coupled to cyclic plasticity in an energetic formulation

Jacinto Ulloa^a, Jef Wambacq^a, Roberto Alessi^b, Geert Degrande^a, Stijn François^a

^a*KU Leuven, Department of Civil Engineering, Kasteelpark Arenberg 40, B-3001 Leuven, Belgium*

^b*Università di Pisa, Department Civil and Industrial Engineering, Largo Lucio Lazzarino, 56122 Pisa, Italy*

Abstract

This paper presents a modeling framework to describe the driving mechanisms of cyclic failure in brittle and ductile materials, including cyclic plasticity and fatigue crack growth. A variational model is devised using the energetic formulation for rate-independent systems, coupling a phase-field description of fatigue fracture to a cyclic plasticity model that includes multi-surface kinematic hardening, gradient-enhanced isotropic hardening/softening and ratcheting. The coupled model embeds two distinctive fatigue effects. The first captures the characteristic features of low-cycle fatigue, driven by the accumulation of plastic strains, while the second accounts for high-cycle fatigue, driven by free energy accumulation. The interplay between these mechanisms allows to describe a wide range of cyclic responses under both force control and displacement control, as shown in several numerical simulations. Moreover, the phase-field approach to fracture accounts for the initiation and complex propagation of fatigue-induced cracks.

Keywords: Fatigue crack growth, Cyclic plasticity, Ratcheting, Damage/phase-field models, Energetic/variational formulation, Gradient-extended internal variables

1. Introduction

Solids and structures subjected to cyclic loading exhibit a progressive reduction in load-carrying capacity due to material degradation. This phenomenon is particularly important in several branches of engineering, accounting for (up to) 90% of all structural failures [1]. Despite its importance, the study of cyclic failure, including cyclic plasticity and various fatigue regimes, remains an open issue in computational mechanics. In particular, models that consistently describe the dissipative behavior of cyclically deforming materials and the evolution of fatigue cracks are significantly limited. In this context, the objective of this study is to propose a model to describe cyclic failure in brittle and ductile materials using a mathematically and physically sound variational framework, and to demonstrate its capabilities in benchmark numerical simulations.

Depending on the loading conditions and material properties, different fatigue regimes can be distinguished [2]. At load amplitudes above a certain threshold, yet small enough to avoid plastic strains, high-

*Corresponding author: Jacinto Ulloa

Email addresses: jacintoisrael.ulloa@kuleuven.be (Jacinto Ulloa), jef.wambacq@kuleuven.be (Jef Wambacq), roberto.alessi@unipi.it (Roberto Alessi), geert.degrande@kuleuven.be (Geert Degrande), stijn.francois@kuleuven.be (Stijn François)

cycle fatigue occurs, governed by a slow material degradation that leads to brittle fractures. Under higher load amplitudes, low-cycle fatigue occurs, driven by a combination of damage and plastic strains, where the initial cyclic response can be rather complex. In particular, cyclic hardening or cyclic softening effects are generally observed, as well as asymmetrical-loading effects, such as ratcheting under force control and stress relaxation under displacement control [3–6]. These cyclically plastic responses may occur in a transient fashion, leading to stabilized hysteretic loops. The interplay between these phenomena and material degradation strongly influences material behavior in the low-cycle fatigue regime.

Classical fatigue analyses are based on (semi-) empirical methods, which require extensive data from experimental tests. Fatigue life is commonly assessed using Wöhler curves, relating the applied stress amplitude to the number of cycles to failure in constant-amplitude cyclic loading. Statistical approaches such as the Basquin relation [7] fit empirical equations to Wöhler curves. The drawback of these techniques lies in their empirical nature, requiring tuning of problem-dependent parameters that do not account for the underlying fracture process. In turn, the conventional approach to fatigue fracture is based on Paris’ law [8] and its extensions [9, 10], which predict crack growth rate as a function of stress intensity factors. Paris’ law is rooted in classical fracture mechanics and is therefore unable to describe crack initiation and the final rupture stage. An alternative approach to fatigue consists of introducing fatigue effects in constitutive material models [11], providing a more versatile framework [12]. However, most models include parameters with no clear physical interpretation, and often use Paris-type laws and Wöhler curves as inputs rather than outputs [13].

This study adopts the framework of constitutive models with non-local internal variables. To properly describe failure modes, such as brittle and quasi-brittle fractures, or shear bands in ductile materials, a suitable representation of highly localized strains is required. Strain localization is captured by models with softening behavior, which, however, render the mathematical problem ill-posed and result in pathological mesh-dependence in numerical simulations. To alleviate these issues, regularization can be introduced by means of non-local effects that are governed by internal length scales. Gradient-enhanced models, as outlined in the formulations of Maugin [14] and Miehe [15], are common examples of this approach.

Developments in the modeling of crack nucleation and propagation have taken place in the last two decades due to the variational approach to fracture [16–18], which links classical fracture mechanics to gradient-damage models. Specifically, the Γ -converging regularization of Bourdin et al. [17] towards the brittle fracture energy functional of Francfort and Marigo [16] provides the basis for the phase-field approach to fracture [19–21], which can be viewed as a particular case of gradient-damage models [22–25]. This framework is able to naturally predict crack initiation and propagation in complex crack topologies, overcoming limitations of classical fracture mechanics and discrete-crack approaches, such as XFEM-based methods [26–28]. While initially developed for brittle fracture, the phase-field approach has been extended to incorporate a variety of material models [29].

Two extensions of the phase-field approach to fracture are particularly relevant for the purposes of this

work. The first is the coupling of the phase field to plasticity [30–41], which allows to describe the nucleation and propagation of ductile cracks. The second is the extension to fatigue that has gained attention in the recent literature [12, 13, 42–44], which has shown to consistently recover Wöhler curves and Paris’ law as post-processing results. Nevertheless, extensions of phase-field-based fatigue to account for the main features of low-cycle fatigue are still missing. In particular, a suitable representation of low-cycle fatigue must include cyclic plasticity, where most theories [5, 45–48] can be linked to the Armstrong–Frederick model [49, 50].

The governing equations of a large class of material models can be derived from the theory of generalized standard materials [51–54]. In this setting, the evolution problem follows from an internal energy density and a dissipation potential, ensuring an a priori fulfilment of the second law of thermodynamics. This theory can be reformulated in a variational setting, where the governing equations emerge as the Euler-Lagrange equations of an energy minimization principle that can be solved using numerical optimization techniques. The pioneering works in this context focused on rate-type variational principles for local elasto-plasticity [55–61], and have been extended to, e.g., gradient-enhanced models [15, 62–64]. In these works, the principle of virtual power is generally used to derive the governing equations [15, 65, 66].

The energetic formulation [67, 68] is a particularly attractive variational framework that furnishes a unified and rigorous mathematical setting for rate-independent dissipative processes. The theory handles non-smooth evolutions (discontinuities in space and time), since no derivatives appear in the most general setting, and provides tools for the analysis of structural and material stability [69]. Some applications of the energetic formulation in the modeling of dissipative solids include plasticity [70, 71], (quasi-)brittle [18, 22, 24, 72] and ductile [30, 38, 39, 73] fracture, shape-memory alloys [74, 75] and fatigue [12, 13].

An important drawback of the theory of generalized standard materials and its variational formulation is the need to enforce the principle of maximum dissipation, which yields evolution laws that comply with the normality condition, thus precluding, in principle, non-associative models. Nevertheless, extensions to non-associativity can be made by introducing state-dependent dissipation potentials. References in this line of work include [72, 76–79]. These developments are essential from a practical standpoint because a variational structure is no longer restricted to associative models, accounting for more realistic representations of, for instance, plasticity in geomaterials and in metals under cyclic loading.

In the framework of the energetic formulation, we propose a model that couples the phase-field approach to fatigue, as suggested by Alessi et al. [12] and Carrara et al. [13], to the main mechanisms of cyclic plasticity. The proposed model includes multi-surface kinematic hardening and a non-associative ratcheting variable [48], as well as gradient-enhanced isotropic hardening/softening. The coupling of the fatigue process to cyclic plasticity renders a general framework that encompasses the characteristic behavior of both high- and low-cycle fatigue in a thermodynamically consistent setting.

This paper is organized as follows. To establish the modeling framework, section 2 presents the energetic formulation applied to a general class of dissipative solids with gradient-enhanced internal variables. These concepts are then used to construct the fatigue model with cyclic plasticity in section 3, with numerical

experiments presented in section 4.

We employ the following notations. Vector- and tensor-valued quantities are denoted with bold symbols, while scalar-valued quantities take non-bold italic symbols. Functionals are denoted by calligraphic upper-case letters. Functions and function values are denoted using the same symbol, such that \square is a space-time-dependent function, evaluated, for instance, as $\square(\mathbf{x}, t)$. Time-dependent functions evaluated at a point in space are denoted with a vector argument, such as $\square(\mathbf{x})$, while space-dependent functions parametrized by time are denoted with a scalar argument, such as $\square(t)$. These distinctions are made when required for clarity purposes, and are otherwise omitted and inferred from context. Finally, an overdot, i.e., $\dot{\square}$, is used to denote the derivative with respect to time, while the symbol ∇ is used to denote the spatial gradient.

2. Variational framework

2.1. Problem outline

Consider an arbitrary solid of mass density ρ occupying a domain $\Omega \subset \mathbb{R}^d$ of dimension $d \in \{1, 2, 3\}$, with boundary $\Gamma \subset \mathbb{R}^{d-1}$. The boundary consists of a Dirichlet part Γ_D with imposed displacements $\bar{\mathbf{u}}(\mathbf{x}, t) \in \mathbb{R}^d$ and a Neumann part Γ_N with imposed tractions $\bar{\mathbf{t}}(\mathbf{x}, t) \in \mathbb{R}^d$, such that $\Gamma_D \cup \Gamma_N = \Gamma$ and $\Gamma_D \cap \Gamma_N = \emptyset$. The solid is also subjected to volume forces per unit mass, denoted as $\mathbf{b}(\mathbf{x}, t) \in \mathbb{R}^d$.

The deformation process is assumed to be quasi-static, occurring in a pseudo-time (loading) interval $I := [0, t_{\max}]$. The displacement field is given by

$$\mathbf{u}: \begin{cases} \Omega \times I \rightarrow \mathbb{R}^d, \\ (\mathbf{x}, t) \mapsto \mathbf{u}(\mathbf{x}, t), \end{cases}$$

which is kinematically admissible, satisfying boundary conditions on Γ_D . Assuming the small-strain hypothesis, the compatible strain tensor $\boldsymbol{\varepsilon}(\mathbf{x}, t) \in \mathbb{R}_{\text{sym}}^{d \times d} := \{\mathbf{e} \mid \mathbf{e} \in \mathbb{R}^{d \times d}, \mathbf{e} = \mathbf{e}^T\}$ is obtained from

$$\boldsymbol{\varepsilon} := \nabla^s \mathbf{u}, \quad \text{with} \quad \nabla^s \mathbf{u} := \frac{1}{2}(\nabla \otimes \mathbf{u} + \mathbf{u} \otimes \nabla).$$

The Cauchy stress tensor $\boldsymbol{\sigma}(\mathbf{x}, t) \in \mathbb{R}_{\text{sym}}^{d \times d}$ is statically admissible, satisfying equilibrium for all $t \in I$:

$$\nabla \cdot \boldsymbol{\sigma} + \rho \mathbf{b} = \mathbf{0} \quad \text{in} \quad \Omega \quad \text{and} \quad \boldsymbol{\sigma} \cdot \mathbf{n} = \bar{\mathbf{t}} \quad \text{on} \quad \Gamma_N, \quad \text{with} \quad \mathbf{u} = \bar{\mathbf{u}} \quad \text{on} \quad \Gamma_D. \quad (1)$$

The dissipative mechanisms that lead to inelastic material behavior are characterized by a generic set of internal variables and their spatial gradients:

$$\mathbf{a}: \begin{cases} \Omega \times I \rightarrow \mathbb{R}^m, \\ (\mathbf{x}, t) \mapsto \mathbf{a}(\mathbf{x}, t), \end{cases} \quad \nabla \mathbf{a}: \begin{cases} \Omega \times I \rightarrow \mathbb{R}^{md}, \\ (\mathbf{x}, t) \mapsto \nabla \mathbf{a}(\mathbf{x}, t). \end{cases}$$

We denote the set of primary fields by $\mathbf{q} := \{\mathbf{u}, \mathbf{a}\}$ and the constitutive state by $\mathbf{c} := \{\boldsymbol{\varepsilon}, \mathbf{a}, \nabla \mathbf{a}\}$. Here, \mathbf{a} is a vector arrangement of m components associated to both scalar- and tensor-valued internal variables.

2.2. Generalized standard materials

Let $\psi := \psi(\boldsymbol{\varepsilon}, \mathbf{a}, \nabla \mathbf{a})$ denote a Helmholtz-type internal energy density. To ensure physical soundness, the second law of thermodynamics is taken as an a priori restriction, given, for isothermal processes, by the Clausius-Planck inequality

$$\boldsymbol{\sigma} : \dot{\boldsymbol{\varepsilon}} - \dot{\psi}(\boldsymbol{\varepsilon}, \mathbf{a}, \nabla \mathbf{a}) \geq 0. \quad (2)$$

The constitutive stress-strain relation

$$\boldsymbol{\sigma} = \frac{\partial \psi}{\partial \boldsymbol{\varepsilon}}(\boldsymbol{\varepsilon}, \mathbf{a}, \nabla \mathbf{a}) \quad (3)$$

directly follows from equation (2), along with the dissipation rate inequality

$$\phi = \mathbf{s} \cdot \dot{\mathbf{a}} \geq 0, \quad \text{with} \quad \mathbf{s} = -\delta_{\mathbf{a}} \psi(\boldsymbol{\varepsilon}, \mathbf{a}, \nabla \mathbf{a}). \quad (4)$$

The set \mathbf{s} contains the thermodynamic forces, or generalized stresses, conjugate to \mathbf{a} , where the operator $\delta_{\square} := \partial_{\square} - \nabla \cdot \partial_{\nabla \square}$ denotes the spatial Euler-Lagrange derivative with respect to \square .

A thermodynamically admissible dissipation potential is defined as $\phi := \phi(\dot{\mathbf{a}}, \nabla \dot{\mathbf{a}}; \mathbf{c}) \geq 0$, which is assumed to be convex with respect to $\{\dot{\mathbf{a}}, \nabla \dot{\mathbf{a}}\}$ and to vanish for null rates. As first conceived by Germain et al. [53], the dependence of the dissipation potential on the state \mathbf{c} accounts for a wide class of material models, including non-associative flow rules [72, 79, 80]. In addition, the dissipation potential may depend on history variables, not included in \mathbf{q} , derived from the time history of the constitutive state, as for the model proposed in section 3. For notational simplicity and without losing generality, this dependence is omitted (but assumed) in the general formulation presented in this section. For rate-independent processes, ϕ is a homogeneous function of first degree in $\{\dot{\mathbf{a}}, \nabla \dot{\mathbf{a}}\}$, such that

$$\phi(b\dot{\mathbf{a}}, b\nabla \dot{\mathbf{a}}; \mathbf{c}) = b\phi(\dot{\mathbf{a}}, \nabla \dot{\mathbf{a}}; \mathbf{c}), \quad \forall b \geq 0.$$

As a consequence, ϕ is not differentiable at null rates, and, from equation (4), it follows that

$$\mathbf{s} \in \partial_{\dot{\mathbf{a}}} \phi(\dot{\mathbf{a}}, \nabla \dot{\mathbf{a}}; \mathbf{c}) - \nabla \cdot \partial_{\nabla \dot{\mathbf{a}}} \phi(\dot{\mathbf{a}}, \nabla \dot{\mathbf{a}}; \mathbf{c}),$$

where $\partial_{\dot{\mathbf{a}}} \phi$ is understood as the multi-valued sub-differential of ϕ . The evolution of \mathbf{a} then takes the form

$$-\delta_{\mathbf{a}} \psi(\boldsymbol{\varepsilon}, \mathbf{a}, \nabla \mathbf{a}) - \delta_{\dot{\mathbf{a}}} \phi(\dot{\mathbf{a}}, \nabla \dot{\mathbf{a}}; \mathbf{c}) \in \mathbf{0}, \quad (5)$$

which is often referred to as Biot's equation (cf. [81]). Equations (1) and (5) represent the strong form of the evolution problem of a general dissipative material model with gradient-enhanced internal variables.

2.3. Energetic formulation

In this section, the governing equations of the evolution problem are recovered in a variational setting. To this end, the basic energy quantities are first introduced in global form. Then, the evolution problem is defined in terms of the energetic formulation for rate-independent systems [68], based on notions of energy balance and stability. These principles naturally lead to an incremental energy minimization problem and constitute the building blocks of the variational fatigue model presented in section 3.

2.3.1. Energy quantities

To characterize how the system stores and dissipates energy in exchange with the external environment, the energetic formulation begins with the definition of global energy functionals. To this end, we denote a general function space of internal variables by \mathcal{A} and the corresponding space of admissible variations that embeds evolution constraints (e.g., irreversibility conditions) by $\tilde{\mathcal{A}}$. The specific form of these function spaces depends on the material model, as will be clear in section 3. The space of kinematically admissible displacement fields and the corresponding space of admissible variations are given by

$$\mathcal{U}(t) := \{\mathbf{w} \in \mathcal{F} \mid \mathbf{w} = \bar{\mathbf{u}}(t) \text{ on } \Gamma_D\} \quad \text{and} \quad \tilde{\mathcal{U}} := \{\tilde{\mathbf{w}} \in \mathcal{F} \mid \tilde{\mathbf{w}} = \mathbf{0} \text{ on } \Gamma_D\}, \quad (6)$$

where the form of \mathcal{F} also depends on the model and is specified in section 3. The space of primary fields then reads $\mathcal{Q} := \mathcal{U} \times \mathcal{A}$, such that $\mathbf{q}(t) \in \mathcal{Q}$ is a process with admissible variations in $\tilde{\mathcal{Q}} := \tilde{\mathcal{U}} \times \tilde{\mathcal{A}}$.

The stored internal energy functional $\mathcal{E}: \mathcal{Q} \rightarrow \mathbb{R} \cup \{+\infty\}$ is given by the state function

$$\mathcal{E}(\mathbf{q}) := \int_{\Omega} \psi(\boldsymbol{\varepsilon}(\mathbf{x}), \mathbf{a}(\mathbf{x}), \nabla \mathbf{a}(\mathbf{x})) \, d\mathbf{x}, \quad (7)$$

while the work of external actions is defined as the time-integral of the external power, namely:

$$\mathcal{L}(\mathbf{u}; [0, t]) := \int_0^t \left[\int_{\Omega} \rho \mathbf{b}(\mathbf{x}, \tau) \cdot \dot{\mathbf{u}}(\mathbf{x}, \tau) \, d\mathbf{x} + \int_{\Gamma_N} \bar{\mathbf{t}}(\mathbf{x}, \tau) \cdot \dot{\mathbf{u}}(\mathbf{x}, \tau) \, d\mathbf{x} + \int_{\Gamma_D} \mathbf{t}_r(\mathbf{x}, \tau) \cdot \dot{\mathbf{u}}(\mathbf{x}, \tau) \, d\mathbf{x} \right] d\tau, \quad (8)$$

where \mathbf{t}_r are the reaction forces on Γ_D . To formulate a stability condition, we introduce the external work distance $\mathcal{T}: I \times \mathcal{U} \times \mathcal{U} \rightarrow \mathbb{R}$, that is, the work done by the external forces at a given time between two admissible states $\{\mathbf{u}_0, \mathbf{u}_1\}$:

$$\mathcal{T}(t, \mathbf{u}_0, \mathbf{u}_1) = \int_{\Omega} \rho \mathbf{b}(\mathbf{x}, t) \cdot (\mathbf{u}_1(\mathbf{x}) - \mathbf{u}_0(\mathbf{x})) \, d\mathbf{x} + \int_{\Gamma_N} \bar{\mathbf{t}}(\mathbf{x}, t) \cdot (\mathbf{u}_1(\mathbf{x}) - \mathbf{u}_0(\mathbf{x})) \, d\mathbf{x}. \quad (9)$$

On the other hand, the dissipative power functional $\mathcal{R}: \tilde{\mathcal{A}} \times \mathcal{Q} \rightarrow [0, +\infty]$ is defined as

$$\mathcal{R}(\dot{\mathbf{a}}; \mathbf{q}) := \int_{\Omega} \phi(\dot{\mathbf{a}}(\mathbf{x}), \nabla \dot{\mathbf{a}}(\mathbf{x}); \mathbf{c}(\mathbf{x})) \, d\mathbf{x}, \quad (10)$$

while the dissipation distance $\mathcal{D}: \mathcal{Q} \times \mathcal{Q} \rightarrow [0, +\infty]$ between two states $\{\mathbf{q}_0, \mathbf{q}_1\}$ reads

$$\mathcal{D}(\mathbf{q}_0, \mathbf{q}_1) := \int_{\Omega} \inf \left\{ \int_0^1 \phi(\dot{\mathbf{a}}(\mathbf{x}, s), \nabla \dot{\mathbf{a}}(\mathbf{x}, s); \mathbf{c}(\mathbf{x}, s)) \, ds \mid \mathbf{q} \in C^1(\Omega \times [0, 1], Q), \mathbf{q}(0) = \mathbf{q}_0, \mathbf{q}(1) = \mathbf{q}_1 \right\} d\mathbf{x}, \quad (11)$$

with $Q \subset \mathbb{R}^d \times \mathbb{R}^m$. This quantity allows to measure the energy dissipated along arbitrary minimizing paths $\mathbf{q}(s) \in \mathcal{Q}$. For smooth evolutions, the total energy dissipated in $[0, t]$ reads

$$\text{Diss}_{\mathcal{D}}(\mathbf{q}; [0, t]) \equiv \int_0^t \mathcal{R}(\dot{\mathbf{a}}(\tau); \mathbf{q}(\tau)) \, d\tau. \quad (12)$$

For certain dissipation potentials obtained as the time-derivative of an energy function, the dissipated energy is a state function [24, 73]. However, as in the present study, this quantity is generally path-dependent.

2.3.2. Evolution problem

From the basic energy quantities, the evolution problem can be defined in variational form by means of the energetic formulation. This framework is based on a notion of energy balance and either a global or a local stability condition, and is directly related to the incremental energy minimization problem of section 2.4.

Global formulation. A process $\mathbf{q}: I \rightarrow \mathcal{Q}$ is an energetic solution if for all $t \in I$:

$$\mathcal{E}(\mathbf{q}(t)) \leq \mathcal{E}(\tilde{\mathbf{q}}) - \mathcal{T}(t, \mathbf{u}(t), \tilde{\mathbf{u}}) + \mathcal{D}(\mathbf{q}(t), \tilde{\mathbf{q}}), \quad \forall \tilde{\mathbf{q}} = \{\tilde{\mathbf{u}}, \tilde{\mathbf{a}}\} \in \mathcal{Q}, \quad (13)$$

$$\mathcal{E}(\mathbf{q}(t)) + \text{Diss}_{\mathcal{D}}(\mathbf{q}; [0, t]) = \mathcal{E}(\mathbf{q}(0)) + \mathcal{L}(\mathbf{u}; [0, t]). \quad (14)$$

Equations (13) and (14) represent, respectively, the global stability condition and global energy balance, and constitute the most general form of the energetic formulation, with regularity assumptions only required for the external loading functions.

Local formulation. To recover the local governing equations (1) and (5), we depart from the notion of global stability and admit, as candidate solutions, those satisfying a local-directional stability condition. For this purpose, let $h \in \mathbb{R}$ denote a variation parameter and $\tilde{\mathbf{q}} \in \tilde{\mathcal{Q}}$ be test directions in which admissible variations on \mathbf{q} take place. Then, a process $\mathbf{q}: [0, t] \rightarrow \mathcal{Q}$ is locally stable if for all $t \in I$, there exists $\bar{h} > 0$ such that

$$\mathcal{E}(\mathbf{q}(t)) \leq \mathcal{E}(\mathbf{q}(t) + h\tilde{\mathbf{q}}) - \mathcal{T}(t, \mathbf{u}(t), \mathbf{u}(t) + h\tilde{\mathbf{u}}) + \mathcal{D}(\mathbf{q}(t), \mathbf{q}(t) + h\tilde{\mathbf{q}}), \quad \forall \tilde{\mathbf{q}} = \{\tilde{\mathbf{u}}, \tilde{\mathbf{a}}\} \in \tilde{\mathcal{Q}}, \quad \forall h \in [0, \bar{h}]. \quad (15)$$

In the context of local stability, it seems reasonable to consider variations in a small neighborhood of the current state, and, due to fatigue conditions, to restrict the test directions to monotonic radial (straight) paths [74]. In this case, the dissipation distance (11) specializes to

$$\mathcal{D}(\mathbf{q}_0, \mathbf{q}_1) = \int_{\Omega} \left\{ \int_0^1 \phi(\dot{\mathbf{a}}(\mathbf{x}, s), \nabla \dot{\mathbf{a}}(\mathbf{x}, s); \mathbf{c}(\mathbf{x}, s)) \, ds \mid \mathbf{q}(s) = \mathbf{q}_0 + s(\mathbf{q}_1 - \mathbf{q}_0) \right\} \, d\mathbf{x}. \quad (16)$$

Assuming that the functionals are Gâteaux-differentiable up to a certain order, a differential stability condition can be defined by replacing the right-hand side of the directional stability condition (15) by a Taylor expansion, and enforcing necessary and sufficient conditions of increasing order for the inequality (15) to hold true [22, 74]. In this sense, a first-order condition is obtained by the functional derivatives

$$\left. \frac{d}{dh} \mathcal{E}(\mathbf{q} + h\tilde{\mathbf{q}}) \right|_{h=0} - \left. \frac{d}{dh} \mathcal{T}(t, \mathbf{u}, \mathbf{u} + h\tilde{\mathbf{u}}) \right|_{h=0} + \left. \frac{d}{dh} \mathcal{D}(\mathbf{q}, \mathbf{q} + h\tilde{\mathbf{q}}) \right|_{h=0} \geq 0, \quad \forall \tilde{\mathbf{q}} \in \tilde{\mathcal{Q}}. \quad (17)$$

As in equation (17), for notational simplicity, implicit dependence on time (and space) will be omitted hereafter, unless required for clarity purposes. Using the first-order homogeneity of the dissipation potential,

we evaluate the Gâteaux derivative of the dissipation distance as

$$\begin{aligned}
\left. \frac{d}{dh} \mathcal{D}(\mathbf{q}, \mathbf{q} + h\tilde{\mathbf{q}}) \right|_{h=0} &= \lim_{h \rightarrow 0} \frac{\mathcal{D}(\mathbf{q}, \mathbf{q} + h\tilde{\mathbf{q}})}{h} \\
&= \lim_{h \rightarrow 0} \frac{1}{h} \int_{\Omega} \left\{ \int_0^1 \phi(\dot{\mathbf{a}}(\mathbf{x}, s), \nabla \dot{\mathbf{a}}(\mathbf{x}, s); \mathbf{c}(\mathbf{x}, s)) ds \mid \mathbf{q}(s) = \mathbf{q} + hs\tilde{\mathbf{q}} \right\} d\mathbf{x} \\
&= \lim_{h \rightarrow 0} \frac{1}{h} \int_{\Omega} \left\{ \int_0^h \phi(\dot{\mathbf{a}}(\mathbf{x}, r), \nabla \dot{\mathbf{a}}(\mathbf{x}, r); \mathbf{c}(\mathbf{x}, r)) dr \mid \mathbf{q}(r) = \mathbf{q} + r\tilde{\mathbf{q}} \right\} d\mathbf{x} \quad (18) \\
&= \lim_{h \rightarrow 0} \frac{1}{h} \int_{\Omega} \int_0^h \phi(\tilde{\mathbf{a}}, \nabla \tilde{\mathbf{a}}; \mathbf{c} + r\tilde{\mathbf{c}}) dr d\mathbf{x} \\
&= \int_{\Omega} \phi(\tilde{\mathbf{a}}, \nabla \tilde{\mathbf{a}}; \mathbf{c}) d\mathbf{x},
\end{aligned}$$

where the change of variable $r = hs$ has been used. Using this result in equation (17) leads to the first-order stability condition

$$\delta \mathcal{E}(\mathbf{q})(\tilde{\mathbf{q}}) + \mathcal{R}(\tilde{\mathbf{a}}; \mathbf{q}) - \int_{\Omega} \rho \mathbf{b} \cdot \tilde{\mathbf{u}} d\mathbf{x} - \int_{\Gamma_N} \bar{\mathbf{t}} \cdot \tilde{\mathbf{u}} d\mathbf{x} \geq 0, \quad \forall \tilde{\mathbf{q}} \in \tilde{\mathcal{Q}}, \quad (19)$$

where $\delta \mathcal{E}(\mathbf{q})(\tilde{\mathbf{q}})$ is the Gâteaux derivative of \mathcal{E} in the direction $\tilde{\mathbf{q}}$. Equation (19) is a necessary condition for directional stability (15) that becomes sufficient if the inequality is strict. Otherwise, the study of higher-order conditions is required [23, 24, 74, 75], which is out of scope in the present study. Furthermore, if the energy quantities in the energy balance (14) are sufficiently regular in $[0, t]$, the time derivative of (14) yields the power balance equation

$$\frac{d}{dt} \mathcal{E}(\mathbf{q}) + \mathcal{R}(\dot{\mathbf{a}}; \mathbf{q}) - \int_{\Omega} \rho \mathbf{b} \cdot \dot{\mathbf{u}} d\mathbf{x} + \int_{\Gamma_N} \bar{\mathbf{t}} \cdot \dot{\mathbf{u}} - \int_{\Gamma_D} \mathbf{t}_r \cdot \dot{\mathbf{u}} d\mathbf{x} = 0. \quad (20)$$

Dissipation inequality. To ensure physical soundness, a dissipation inequality is included in the formulation [69], ensuring the fulfilment of the second law of thermodynamics:

$$\phi(\dot{\mathbf{a}}, \nabla \dot{\mathbf{a}}; \mathbf{c}) \geq 0 \quad \text{in } \Omega \times I. \quad (21)$$

Governing equations. Using equations (7)–(10), and in view of the stress-strain relation (3), the first-order stability condition (19) yields

$$\begin{aligned}
\int_{\Omega} \{ \delta_{\mathbf{a}} \psi(\boldsymbol{\varepsilon}, \mathbf{a}, \nabla \mathbf{a}) + \delta_{\tilde{\mathbf{a}}} \phi(\tilde{\mathbf{a}}, \nabla \tilde{\mathbf{a}}; \mathbf{q}) \} \cdot \tilde{\mathbf{a}} d\mathbf{x} + \int_{\Gamma} \{ \mathbf{n} \cdot (\partial_{\nabla \tilde{\mathbf{a}}} \phi(\tilde{\mathbf{a}}, \nabla \tilde{\mathbf{a}}; \mathbf{q}) + \partial_{\nabla \mathbf{a}} \psi(\boldsymbol{\varepsilon}, \mathbf{a}, \nabla \mathbf{a})) \} \cdot \tilde{\mathbf{a}} d\mathbf{x} \\
- \int_{\Omega} (\nabla \cdot \boldsymbol{\sigma} + \rho \mathbf{b}) \cdot \tilde{\mathbf{u}} d\mathbf{x} + \int_{\Gamma_N} (\boldsymbol{\sigma} \cdot \mathbf{n} - \bar{\mathbf{t}}) \cdot \tilde{\mathbf{u}} d\mathbf{x} \geq 0, \quad (22)
\end{aligned}$$

which holds for all $\tilde{\mathbf{q}} \in \tilde{\mathcal{Q}}$. Likewise, the power balance (20) gives

$$\begin{aligned}
\int_{\Omega} \{ \delta_{\mathbf{a}} \psi(\boldsymbol{\varepsilon}, \mathbf{a}, \nabla \mathbf{a}) + \delta_{\dot{\mathbf{a}}} \phi(\dot{\mathbf{a}}, \nabla \dot{\mathbf{a}}; \mathbf{q}) \} \cdot \dot{\mathbf{a}} d\mathbf{x} + \int_{\Gamma} \{ \mathbf{n} \cdot (\partial_{\nabla \dot{\mathbf{a}}} \phi(\dot{\mathbf{a}}, \nabla \dot{\mathbf{a}}; \mathbf{q}) + \partial_{\nabla \mathbf{a}} \psi(\boldsymbol{\varepsilon}, \mathbf{a}, \nabla \mathbf{a})) \} \cdot \dot{\mathbf{a}} d\mathbf{x} \\
- \int_{\Omega} (\nabla \cdot \boldsymbol{\sigma} + \rho \mathbf{b}) \cdot \dot{\mathbf{u}} d\mathbf{x} + \int_{\Gamma_N} (\boldsymbol{\sigma} \cdot \mathbf{n} - \bar{\mathbf{t}}) \cdot \dot{\mathbf{u}} d\mathbf{x} + \int_{\Gamma_D} (\boldsymbol{\sigma} \cdot \mathbf{n} - \mathbf{t}_r) \cdot \dot{\mathbf{u}} d\mathbf{x} = 0. \quad (23)
\end{aligned}$$

Equations (22) and (23) yield:

$$\left\{ \begin{array}{ll} \nabla \cdot \boldsymbol{\sigma} + \rho \mathbf{b} = \mathbf{0} & \text{in } \Omega, \\ \boldsymbol{\sigma} \cdot \mathbf{n} = \bar{\mathbf{t}} & \text{on } \Gamma_N, \\ \boldsymbol{\sigma} \cdot \mathbf{n} = \mathbf{t}_r & \text{on } \Gamma_D, \end{array} \right. \quad \text{and} \quad \left\{ \begin{array}{ll} -\delta_{\mathbf{a}} \psi(\boldsymbol{\varepsilon}, \mathbf{a}, \nabla \mathbf{a}) - \delta_{\tilde{\mathbf{a}}} \phi(\tilde{\mathbf{a}}, \nabla \tilde{\mathbf{a}}; \mathbf{q}) \leq \mathbf{0} & \text{in } \Omega, \\ \{ -\delta_{\mathbf{a}} \psi(\boldsymbol{\varepsilon}, \mathbf{a}, \nabla \mathbf{a}) - \delta_{\dot{\mathbf{a}}} \phi(\dot{\mathbf{a}}, \nabla \dot{\mathbf{a}}; \mathbf{q}) \} \cdot \dot{\mathbf{a}} = 0 & \text{in } \Omega, \\ \nabla \mathbf{a} \cdot \mathbf{n} = \mathbf{0} & \text{on } \Gamma, \end{array} \right. \quad (24)$$

which recover the equilibrium equations (1) and, along with the dissipation inequality (21), the evolution equations (5) for internal variables with boundary conditions.

2.4. Incremental minimization problem

An incremental minimization problem suitable for numerical implementation follows from the global form of the energetic formulation [68]. Consider $n_t + 1$ discrete time instants $0 = t_0 < \dots < t_n < t_{n+1} < \dots < t_{n_t} = t_{\max}$. In view of equation (16), the incremental dissipated energy up to t_{n+1} is given by

$$\mathcal{D}(\mathbf{q}_0, \mathbf{q}_{n+1}) = \mathcal{D}(\mathbf{q}_0, \mathbf{q}_n) + \int_{\Omega} \int_{t_n}^{t_{n+1}} \phi \left(\frac{\mathbf{a}_{n+1} - \mathbf{a}_n}{t_{n+1} - t_n}, \frac{\nabla \mathbf{a}_{n+1} - \nabla \mathbf{a}_n}{t_{n+1} - t_n}; \mathbf{c}_n + \frac{t - t_n}{t_{n+1} - t_n} (\mathbf{c}_{n+1} - \mathbf{c}_n) \right) dt d\mathbf{x}. \quad (25)$$

To evaluate this quantity in the general case of path-dependent dissipation potentials, we take the zeroth-order term of a Taylor expansion of the integral kernel in equation (25), noting that all other terms imply rate dependence. This approximation gives $\phi(\mathbf{a}_{n+1} - \mathbf{a}_n, \nabla \mathbf{a}_{n+1} - \nabla \mathbf{a}_n; \mathbf{c}_n)$, such that

$$\mathcal{D}(\mathbf{q}_0, \mathbf{q}_{n+1}) \approx \mathcal{D}_{n+1}(\mathbf{a}_{n+1}) := \mathcal{D}(\mathbf{q}_0, \mathbf{q}_n) + \mathcal{R}(\mathbf{a}_{n+1} - \mathbf{a}_n; \mathbf{q}_n). \quad (26)$$

Assuming all states up to t_n are known, the unknown state \mathbf{q}_{n+1} is found from the variational principle

$$\inf_{\mathbf{q}_{n+1} \in \mathcal{Q}} \{ \mathcal{E}(\mathbf{q}_{n+1}) - \mathcal{P}(\mathbf{u}_{n+1}) + \mathcal{D}_{n+1}(\mathbf{a}_{n+1}) \mid \phi(\mathbf{a}_{n+1} - \mathbf{a}_n, \nabla \mathbf{a}_{n+1} - \nabla \mathbf{a}_n; \mathbf{c}_n) \geq 0 \}. \quad (27)$$

Given a suitable incremental representation of the dissipated energy, the Euler-Lagrange equations of (27) recover the continuous evolution problem as $t_{n+1} - t_n \rightarrow 0$.

3. A phase-field model with fatigue effects coupled to cyclic plasticity

This section presents the proposed model that couples the phase-field approach to fatigue with cyclic plasticity, derived using the concepts presented in section 2. First, the modeling of cyclic plasticity is addressed, where a non-associative ratcheting variable is introduced in the variational framework. Then, the full model is elaborated by introducing the phase-field description of fatigue-induced fracture.

3.1. Modeling cyclic plasticity with ratcheting

To account for cyclic plasticity with ratcheting effects, we take the model of Houlsby et al. [48] as a point of departure, which was proposed to describe the behavior of cyclically loaded pile foundations [82]. The original model is tightly linked to Armstrong and Frederick [49], but allows for multi-surface kinematic hardening with a single ratcheting variable. Herein, we also consider isotropic hardening/softening and gradient-extended plasticity [63, 64, 83–85], accounting for a general class of elastoplastic materials.

To present the model, we adopt the classical setting of plasticity, where auxiliary internal variables are introduced to account for hardening effects [86, 87] and, in this case, ratcheting. As in classical plasticity, the evolution of the internal variables is first presented in dual form, that is, in terms of yield functions in generalized stress space, where the issue of associativity is addressed. Then, a state-dependent, primal dissipation potential is obtained, which is used to construct the coupled fatigue model in section 3.2.

3.1.1. Constitutive model

We focus on a multi-surface representation of the plastic deformation process, with n_y yield surfaces of increasing yield strength. To this end, we introduce the internal variables

$$\{\boldsymbol{\varepsilon}^p, \boldsymbol{\kappa}, \boldsymbol{\varepsilon}^r\}, \quad \text{with} \quad \boldsymbol{\varepsilon}^p := \{\boldsymbol{\varepsilon}_1^p, \dots, \boldsymbol{\varepsilon}_{n_y}^p\} \quad \text{and} \quad \boldsymbol{\kappa} := \{\kappa_1, \dots, \kappa_{n_y}\}. \quad (28)$$

In (28), the subscript s denotes the s^{th} yield surface, $\boldsymbol{\varepsilon}_s^p: \Omega \times I \rightarrow \mathbb{R}_{\text{dev}}^{d \times d} := \{\boldsymbol{e} \in \mathbb{R}_{\text{sym}}^{d \times d}, \text{tr}(\boldsymbol{e}) = 0\}$ is the plastic strain tensor, $\kappa_s: \Omega \times I \rightarrow \mathbb{R}_+$ is an isotropic hardening/softening variable and $\boldsymbol{\varepsilon}^r: \Omega \times I \rightarrow \mathbb{R}_{\text{dev}}^{d \times d}$ is a ratcheting strain tensor. As a modeling assumption, κ_s evolves according to the hardening law:

$$\dot{\kappa}_s := \sqrt{\frac{2}{3}} \|\dot{\boldsymbol{\varepsilon}}_s^p\|, \quad (29)$$

while $\boldsymbol{\varepsilon}^r$ evolves according to the ratcheting law [48]:

$$\dot{\boldsymbol{\varepsilon}}^r := \beta \hat{\boldsymbol{n}}^g \sum_{s=1}^{n_y} \|\dot{\boldsymbol{\varepsilon}}_s^p\|, \quad (30)$$

where $\hat{\boldsymbol{n}}^g := \boldsymbol{\sigma}_{\text{dev}} / \|\boldsymbol{\sigma}_{\text{dev}}\|$ is the direction of the deviatoric stress. The parameter $\beta \in [0, 1]$ defines the fraction of plastic strains that contributes to ratcheting, assumed, for simplicity, to be equal for all yield surfaces.

The free energy density is defined as

$$\psi(\boldsymbol{\varepsilon}, \boldsymbol{\varepsilon}^p, \boldsymbol{\kappa}, \boldsymbol{\varepsilon}^r, \nabla \boldsymbol{\kappa}) := \underbrace{\frac{1}{2} \|\boldsymbol{\varepsilon} - \sum_{s=1}^{n_y} \boldsymbol{\varepsilon}_s^p - \boldsymbol{\varepsilon}^r\|_{\mathbf{C}}^2}_{\psi^e(\boldsymbol{\varepsilon}, \boldsymbol{\varepsilon}^p, \boldsymbol{\varepsilon}^r)} + \underbrace{\frac{1}{2} \sum_{s=1}^{n_y} (H_s^{\text{kin}} \boldsymbol{\varepsilon}_s^p : \boldsymbol{\varepsilon}_s^p + H_s^{\text{iso}} \kappa_s^2) + \frac{1}{2} \eta_p^2 \sum_{s=1}^{n_y} \|\nabla \kappa_s\|^2}_{\psi^p(\boldsymbol{\varepsilon}^p, \boldsymbol{\kappa}, \nabla \boldsymbol{\kappa})}, \quad (31)$$

where \mathbf{C} is the fourth-order elastic tensor, and H_s^{kin} and H_s^{iso} denote the kinematic and isotropic hardening moduli, respectively, for the s^{th} yield surface. The last term in equation (31) introduces non-local effects governed by the plastic internal length scale η_p , which is equal for all yield surfaces for the sake of simplicity.

In view of equation (31), the stress tensor is obtained from equation (3) as

$$\boldsymbol{\sigma}(\boldsymbol{\varepsilon}, \boldsymbol{\varepsilon}^p, \boldsymbol{\varepsilon}^r) = \frac{\partial \psi}{\partial \boldsymbol{\varepsilon}} = \mathbf{C} : \left(\boldsymbol{\varepsilon} - \sum_{s=1}^{n_y} \boldsymbol{\varepsilon}_s^p - \boldsymbol{\varepsilon}^r \right). \quad (32)$$

The generalized stresses conjugate to (28) read

$$\{\boldsymbol{\varsigma}^p, \boldsymbol{h}, \boldsymbol{\varsigma}^r\}, \quad \text{with} \quad \boldsymbol{\varsigma}^p := \{\boldsymbol{\varsigma}_1^p, \dots, \boldsymbol{\varsigma}_{n_y}^p\} \quad \text{and} \quad \boldsymbol{h} := \{h_1, \dots, h_{n_y}\}. \quad (33)$$

These dual variables follow from equation (4) as

$$\boldsymbol{\varsigma}_s^p = -\delta_{\boldsymbol{\varepsilon}_s^p} \psi \equiv \boldsymbol{\sigma} - H_s^{\text{kin}} \boldsymbol{\varepsilon}_s^p, \quad h_s = -\delta_{\kappa_s} \psi \equiv -H_s^{\text{iso}} \kappa_s + \eta_p^2 \nabla \cdot \nabla \kappa_s, \quad \boldsymbol{\varsigma}^r = -\delta_{\boldsymbol{\varepsilon}^r} \psi \equiv \boldsymbol{\sigma}. \quad (34)$$

3.1.2. Dissipation

Focusing on J_2 plasticity, the yield functions are defined in generalized stress space as

$$f_s(\boldsymbol{\varsigma}_s^p, h_s) := \|\boldsymbol{\varsigma}_{s\text{dev}}^p\| - \sqrt{\frac{2}{3}} (\sigma_s^p - h_s) \leq 0, \quad (35)$$

where σ_s^p is the s^{th} plastic yield strength. The set of admissible generalized stresses for each yield surface is the convex set

$$\mathbb{K}_s := \{ \boldsymbol{\varsigma}_s^p, h_s, \boldsymbol{\varsigma}^r \mid f_s(\boldsymbol{\varsigma}_s^p, h_s) \leq 0 \},$$

such that the elastic domain is the intersection of all \mathbb{K}_s , and thus still a convex set:

$$\mathbb{K} := \bigcap_{s=1}^{n_y} \mathbb{K}_s = \{ \boldsymbol{\varsigma}^p, \mathbf{h}, \boldsymbol{\varsigma}^r \mid f_s(\boldsymbol{\varsigma}_s^p, h_s) \leq 0 \ \forall s \in Y \}, \quad (36)$$

where $Y := \mathbb{Z} \cap [1, n_y]$. To obtain the primal representation of dissipation, the dissipation potential is obtained as the support function of \mathbb{K} for given rates $\{\dot{\boldsymbol{\epsilon}}^p, \dot{k}, \dot{\boldsymbol{\epsilon}}^r\}$:

$$\phi = \sup_{\{\boldsymbol{\varsigma}^p, \mathbf{h}, \boldsymbol{\varsigma}^r\} \in \mathbb{K}} \{ \boldsymbol{\varsigma}^p : \dot{\boldsymbol{\epsilon}}^p + \mathbf{h} \cdot \dot{\boldsymbol{\kappa}} + \boldsymbol{\varsigma}^r : \dot{\boldsymbol{\epsilon}}^r \}. \quad (37)$$

This optimization problem can be viewed as a particular statement of the principle of maximum dissipation. Equation (37) yields the associative flow rule for the plastic strains, as well as the associative hardening law, consistent with equation (29) and the normality law [51, 57]:

$$\dot{\boldsymbol{\epsilon}}_s^p = \sum_{k=1}^{n_y} \lambda_k \frac{\partial f_k}{\partial \boldsymbol{\varsigma}_s^p} \equiv \lambda_s \hat{\boldsymbol{n}}_s, \quad \dot{k}_s = \sum_{k=1}^{n_y} \lambda_k \frac{\partial f_k}{\partial h_s} \equiv \sqrt{\frac{2}{3}} \lambda_s, \quad (38)$$

where $\lambda_k \geq 0$ and $\hat{\boldsymbol{n}}_s := \boldsymbol{\varsigma}_{s\text{dev}}^p / \|\boldsymbol{\varsigma}_{s\text{dev}}^p\|$ is the direction of the plastic flow. However, $\partial_{\boldsymbol{\varsigma}^r} f_s = \mathbf{0}$ implies that $\dot{\boldsymbol{\epsilon}}^r \equiv \mathbf{0}$. Therefore, the ratcheting law (30) is not obtained from (37) and is thus considered non-associative. Equation (37) then leads to a dissipation potential that is independent of the ratcheting strain rate.

An approach to circumvent this issue and recover a variational structure in models with non-associative components is to let \mathbb{K} depend on the current state [79]. To this end, we define

$$\mathbb{K}(\boldsymbol{\sigma}) := \{ \boldsymbol{\varsigma}^p, \mathbf{h}, \boldsymbol{\varsigma}^r \mid \hat{f}_s(\boldsymbol{\varsigma}_s^p, h_s, \boldsymbol{\varsigma}^r) - \beta \|\boldsymbol{\sigma}_{\text{dev}}\| \leq 0 \ \forall s \in Y \}, \quad (39)$$

where $\hat{f}_s(\boldsymbol{\varsigma}_s^p, h_s, \boldsymbol{\varsigma}^r) := f_s(\boldsymbol{\varsigma}_s^p, h_s) + \beta \|\boldsymbol{\varsigma}_{\text{dev}}^r\|$. The principle of maximum dissipation is now enforced as

$$\phi = \sup_{\{\boldsymbol{\varsigma}^p, \mathbf{h}, \boldsymbol{\varsigma}^r\} \in \mathbb{K}(\boldsymbol{\sigma})} \{ \boldsymbol{\varsigma}^p : \dot{\boldsymbol{\epsilon}}^p + \mathbf{h} \cdot \dot{\boldsymbol{\kappa}} + \boldsymbol{\varsigma}^r : \dot{\boldsymbol{\epsilon}}^r \}, \quad (40)$$

yielding, again, the evolution equations (38) and a consistent ratcheting flow rule:

$$\dot{\boldsymbol{\epsilon}}^r = \sum_{s=1}^{n_y} \lambda_s \frac{\partial \hat{f}_s}{\partial \boldsymbol{\varsigma}^r} \equiv \beta \hat{\boldsymbol{n}}^g \sum_{s=1}^{n_y} \lambda_s. \quad (41)$$

In equations (38) and (41), we note that the direction of the plastic flow for each yield surface coincides with the direction of the effective deviatoric stress $\boldsymbol{\varsigma}_{s\text{dev}}^p$, while the direction of the ratcheting strain rate coincides with the direction of the deviatoric stress $\boldsymbol{\sigma}_{\text{dev}}$. In view of equations (29)-(30), equation (40) is evaluated as

$$\begin{aligned}
\phi &= \sup \left\{ \boldsymbol{\varsigma}^p : \dot{\boldsymbol{\varepsilon}}^p + \mathbf{h} \cdot \dot{\boldsymbol{\kappa}} + \boldsymbol{\varsigma}^r : \dot{\boldsymbol{\varepsilon}}^r \mid \hat{f}_s(\boldsymbol{\varsigma}_s^p, h_s, \boldsymbol{\varsigma}^r) \leq \beta \|\boldsymbol{\sigma}_{\text{dev}}\| \quad \forall s \in Y \right\} \\
&= \sup \left\{ \sum_{s=1}^{n_y} (\boldsymbol{\varsigma}_s^p : \dot{\boldsymbol{\varepsilon}}_s^p + h_s \dot{\boldsymbol{\kappa}}_s) + \boldsymbol{\varsigma}^r : \dot{\boldsymbol{\varepsilon}}^r \mid \|\boldsymbol{\varsigma}_{s\text{dev}}^p\| + \sqrt{\frac{2}{3}} h_s + \beta \|\boldsymbol{\varsigma}_{\text{dev}}^r\| \leq \sqrt{\frac{2}{3}} \sigma_s^p + \beta \|\boldsymbol{\sigma}_{\text{dev}}\| \quad \forall s \in Y \right\} \\
&= \sup \left\{ \sum_{s=1}^{n_y} \left(\|\boldsymbol{\varsigma}_{s\text{dev}}^p\| + \sqrt{\frac{2}{3}} h_s + \beta \|\boldsymbol{\varsigma}_{\text{dev}}^r\| \right) \|\dot{\boldsymbol{\varepsilon}}_s^p\| \mid \|\boldsymbol{\varsigma}_{s\text{dev}}^p\| + \sqrt{\frac{2}{3}} h_s + \beta \|\boldsymbol{\varsigma}_{\text{dev}}^r\| \leq \sqrt{\frac{2}{3}} \sigma_s^p + \beta \|\boldsymbol{\sigma}_{\text{dev}}\| \quad \forall s \in Y \right\} \\
&= \sum_{s=1}^{n_y} \left(\sqrt{\frac{2}{3}} \sigma_s^p + \beta \|\boldsymbol{\sigma}_{\text{dev}}\| \right) \|\dot{\boldsymbol{\varepsilon}}_s^p\| \equiv \sum_{s=1}^{n_y} \sigma_s^p \dot{\boldsymbol{\kappa}}_s + \boldsymbol{\sigma} : \dot{\boldsymbol{\varepsilon}}^r.
\end{aligned} \tag{42}$$

This expression is consistent with the dissipation potential proposed by Houlsby et al. [48] in the context of hyperplasticity, a topic strongly linked to generalized standard materials [80].

3.2. Coupling cyclic plasticity to a phase-field approach to fatigue

3.2.1. Constitutive model

The formulation is now extended, coupling the cyclic plasticity model to a phase-field description of fatigue fracture. For this purpose, the usual phase-field/damage variable is defined as $\alpha: \Omega \times I \rightarrow [0, 1]$, with $\alpha = 0$ and $\alpha = 1$ corresponding to an undamaged and a fully degraded material state, respectively. Regularization is attained by the gradient of the phase field $\nabla \alpha: \Omega \times I \rightarrow \mathbb{R}^d$. Then, along with the plastic variables introduced in the previous section, the constitutive state reads

$$\mathbf{c} := \{\nabla^s \mathbf{u}, \boldsymbol{\varepsilon}^p, \boldsymbol{\kappa}, \boldsymbol{\varepsilon}^r, \alpha, \nabla \boldsymbol{\kappa}, \nabla \alpha\},$$

with primary fields

$$\mathbf{q} := \{\mathbf{u}, \boldsymbol{\varepsilon}^p, \boldsymbol{\kappa}, \boldsymbol{\varepsilon}^r, \alpha\}.$$

The damage variable is considered irreversible, thus excluding healing evolutions:

$$\dot{\alpha} \geq 0 \quad \text{in} \quad \Omega \times I. \tag{43}$$

Note that from the hardening law (29), it follows that $\boldsymbol{\kappa}_s \subseteq \boldsymbol{\kappa}$ is also irreversible by definition.

Material degradation is achieved by letting the free energy density decrease as a function of α :

$$\psi(\boldsymbol{\varepsilon}, \boldsymbol{\varepsilon}^p, \boldsymbol{\kappa}, \boldsymbol{\varepsilon}^r, \alpha, \nabla \boldsymbol{\kappa}) := g(\alpha) (\psi^{e+}(\boldsymbol{\varepsilon}, \boldsymbol{\varepsilon}^p, \boldsymbol{\varepsilon}^r) + \psi^p(\boldsymbol{\varepsilon}^p, \boldsymbol{\kappa}, \nabla \boldsymbol{\kappa})) + \psi^{e-}(\boldsymbol{\varepsilon}, \boldsymbol{\varepsilon}^p, \boldsymbol{\varepsilon}^r), \tag{44}$$

where $g(\alpha)$ is a damage degradation function endowed with the following properties:

$$g(0) = 1, \quad g(1) = 0, \quad g'(\alpha) \leq 0 \quad \forall \alpha \in [0, 1]. \tag{45}$$

In this work, the widely used quadratic function is adopted:

$$g(\alpha) := (1 - \alpha)^2. \tag{46}$$

In equation (44), ψ^P is the plastic free energy density given in equation (31). In turn, the elastic free energy is split into positive and negative parts, denoted as ψ^{e+} and ψ^{e-} , respectively. This decomposition is introduced to consider anisotropic behavior in tension and compression, and can be performed in different ways. Herein, we consider the volumetric-deviatoric split [88]:

$$\begin{cases} \psi^{e+}(\boldsymbol{\varepsilon}, \boldsymbol{\varepsilon}^P, \boldsymbol{\varepsilon}^r) := \frac{1}{2}K \langle \text{tr}(\boldsymbol{\varepsilon}^e) \rangle_+^2 + \mu(\boldsymbol{\varepsilon}_{\text{dev}}^e : \boldsymbol{\varepsilon}_{\text{dev}}^e), \\ \psi^{e-}(\boldsymbol{\varepsilon}, \boldsymbol{\varepsilon}^P, \boldsymbol{\varepsilon}^r) := \frac{1}{2}K \langle \text{tr}(\boldsymbol{\varepsilon}^e) \rangle_-^2, \end{cases} \quad (47)$$

where K is the bulk modulus, μ is the shear modulus, and

$$\boldsymbol{\varepsilon}^e := \boldsymbol{\varepsilon} - \sum_{s=1}^{n_y} \boldsymbol{\varepsilon}_s^P - \boldsymbol{\varepsilon}^r$$

is the elastic strain tensor. From the decomposed energy density (44), the stress-strain relation (3) reads

$$\boldsymbol{\sigma}(\boldsymbol{\varepsilon}, \boldsymbol{\varepsilon}^P, \boldsymbol{\varepsilon}^r, \alpha) = \frac{\partial \psi}{\partial \boldsymbol{\varepsilon}} = g(\alpha) \frac{\partial \psi^{e+}}{\partial \boldsymbol{\varepsilon}} + \frac{\partial \psi^{e-}}{\partial \boldsymbol{\varepsilon}}. \quad (48)$$

3.2.2. Dissipation

The definition of the dissipation potential should entail the coupling of the plastic strains to the damage evolution, for which we follow the approaches in references [30–32, 38, 39], and extend the formulation to multiple yield surfaces, kinematic hardening and ratcheting. Moreover, following Alessi et al. [12] and Carrara et al. [13], fatigue effects are considered by means of a local fatigue variable, defined here as $\gamma: \Omega \times I \rightarrow \mathbb{R}_+$, and a fatigue degradation function $\gamma \mapsto d(\gamma) \in [0, 1]$. This function has the following properties:

$$d(\gamma \leq \gamma_0) = 1, \quad d(\gamma > \gamma_0) \in [0, 1], \quad d'(\gamma) \leq 0, \quad (49)$$

where γ_0 is a threshold parameter.

The different dissipative ingredients are introduced in the following dissipation potential:

$$\phi(\dot{\boldsymbol{\varepsilon}}^P, \dot{\boldsymbol{\kappa}}, \dot{\boldsymbol{\varepsilon}}^r, \dot{\boldsymbol{a}}, \nabla \dot{\boldsymbol{a}}; \boldsymbol{\kappa}, \alpha, \boldsymbol{\sigma}, \gamma) := \underbrace{\phi^P(\dot{\boldsymbol{\varepsilon}}^P, \dot{\boldsymbol{\kappa}}, \dot{\boldsymbol{\varepsilon}}^r; \alpha, \boldsymbol{\sigma})}_{\text{plastic diss.}} + \sum_{s=1}^{n_y} \underbrace{g'(\alpha) \sigma_s^P \kappa_s \dot{\alpha}}_{\text{coupling}} + \underbrace{\phi^d(\dot{\alpha}, \nabla \dot{\alpha}; \gamma)}_{\text{damage diss.}}, \quad (50)$$

where the irreversibility condition (43) and the plastic flow relations (29)-(30) are assumed a priori. The coupling term $g'(\alpha) \kappa_s \dot{\alpha}$ was introduced by Alessi et al. [32] for perfect plasticity to render the dissipation potential a state function. This idea is also applied here and generalized to the multi-surface hardening case. However, due to the dependence on $\boldsymbol{\sigma}$ and γ , only a part of ϕ becomes path-independent. The plastic dissipation corresponds to the damaged version of equation (42):

$$\phi^P(\dot{\boldsymbol{\varepsilon}}^P, \dot{\boldsymbol{\kappa}}, \dot{\boldsymbol{\varepsilon}}^r; \alpha, \boldsymbol{\sigma}) := \sum_{s=1}^{n_y} g(\alpha) \sigma_s^P \dot{\kappa}_s + \boldsymbol{\sigma}(\boldsymbol{\varepsilon}, \boldsymbol{\varepsilon}^P, \boldsymbol{\varepsilon}^r, \alpha) : \dot{\boldsymbol{\varepsilon}}^r, \quad (51)$$

where dependence on the plastic strain rates is enforced through the hardening and ratcheting rules (29)-(30). The degradation function $g(\alpha)$ is used to let the plastic yield strength decrease as a function of damage. More general choices of functions that comply with (45) are possible, as discussed by Alessi et al. [32]. Herein, we

only consider the quadratic function (46), which is reflected in the coupling term $g'(\alpha)\kappa_s\dot{\alpha}$. The phase-field fracture dissipation with fatigue effects reads

$$\phi^d(\dot{\alpha}, \nabla\dot{\alpha}; \gamma) := d(\gamma)(w'(\alpha)\dot{\alpha} + \eta_d^2 \nabla\alpha \cdot \nabla\dot{\alpha}), \quad (52)$$

where η_d is the damage internal length scale. The terms $w'(\alpha)\dot{\alpha} + \eta_d^2 \nabla\alpha \cdot \nabla\dot{\alpha}$ constitute the standard phase-field dissipation power, whose time integral yields the regularized fracture energy density. This quantity is subject to degradation through $d(\gamma)$, which introduces a path-dependent fatigue effect. The function $w(\alpha)$ represents the local dissipated energy due to damage, for which two models (labeled AT-1 and AT-2 after Ambrosio and Tortorelli [89]) are generally adopted [24]:

$$w(\alpha) := \begin{cases} w_0\alpha & \text{AT-1,} \\ w_0\alpha^2 & \text{AT-2.} \end{cases} \quad (53)$$

While the AT-2 model is used in most studies, the AT-1 model has the advantage of including an initial elastic stage before damage is triggered, where w_0 is a threshold parameter [24, 38]. Regarding the fatigue degradation function, different options have been proposed [12, 13], from which we adopt the following:

$$d(\gamma) := \begin{cases} 1 & \text{if } \gamma(\mathbf{x}, t) \leq \gamma_0, \\ \left[1 - k \log\left(\frac{\gamma(\mathbf{x}, t)}{\gamma_0}\right)\right]^2 & \text{if } \gamma_0 \leq \gamma(\mathbf{x}, t) \leq \gamma_0 10^{1/k}, \\ 0 & \text{otherwise,} \end{cases} \quad (54)$$

where k is a material parameter that controls the rate of (logarithmic) decay of the degradation function. The fatigue variable γ is defined as

$$\gamma(\mathbf{x}, t) := \int_0^t |\dot{\vartheta}(\mathbf{x}, s)| H(\dot{\vartheta}(\mathbf{x}, s)) ds, \quad \text{with } \vartheta(\mathbf{x}, t) := g(\alpha)(\psi^{\text{e+}}(\boldsymbol{\varepsilon}, \boldsymbol{\varepsilon}^{\text{p}}, \boldsymbol{\varepsilon}^{\text{r}}) + \psi^{\text{p}}(\boldsymbol{\varepsilon}^{\text{p}}, \boldsymbol{\kappa}, \nabla\boldsymbol{\kappa})). \quad (55)$$

While other definitions are possible for ϑ , e.g., an accumulated strain measure, using the strain energy density ensures mesh objectivity [13]. Moreover, the Heaviside function H precludes fatigue degradation in unloading stages. Note that in the present model, the plastic free energy also contributes to the evolution of γ .

3.3. Energetic formulation

With the previous definitions, the governing equations of the coupled model can be derived from the principles of the energetic formulation. For this purpose, we define the space of displacement fields in equation (6) by $\mathcal{F} := H^1(\Omega, \mathbb{R}^d)$, and the following function spaces for the internal variables:

$$\mathcal{B} := L^2(\Omega, \mathbb{R}_{\text{dev}}^{d \times d}), \quad \tilde{\mathcal{B}} \equiv \mathcal{B}, \quad (56)$$

$$\mathcal{K} := H^1(\Omega, \mathbb{R}_+), \quad \tilde{\mathcal{K}}(\tilde{\boldsymbol{p}}) := \{\tilde{\xi} \in \mathcal{K} \mid \tilde{\xi} = \|\tilde{\boldsymbol{p}}\|_2, \tilde{\boldsymbol{p}} \in \tilde{\mathcal{B}}\}, \quad (57)$$

$$\mathcal{R} := L^2(\Omega, \mathbb{R}_{\text{dev}}^{d \times d}), \quad \tilde{\mathcal{R}}(\tilde{\xi}, \mathbf{m}) := \{\tilde{\mathbf{r}} \in \mathcal{R} \mid \tilde{\mathbf{r}} = \tilde{\xi}\mathbf{m}, \tilde{\xi} \in \tilde{\mathcal{K}}, \mathbf{m} \in \mathcal{B}\}, \quad (58)$$

$$\mathcal{D} := H^1(\Omega, [0, 1]), \quad \tilde{\mathcal{D}} := H^1(\Omega, \mathbb{R}_+). \quad (59)$$

The accessible primary fields are then given by

$$\mathbf{q} = \{\mathbf{u}, \boldsymbol{\varepsilon}^p, \boldsymbol{\kappa}, \boldsymbol{\varepsilon}^r, \alpha\} \in \mathcal{Q} := \mathcal{U} \times \mathcal{P} \times \mathcal{D}, \quad \text{with} \quad \mathcal{P} := \mathcal{B} \times \cdots \times \mathcal{B} \times \mathcal{K} \times \cdots \times \mathcal{K} \times \mathcal{R}. \quad (60)$$

The space of admissible variations must account for evolution constraints of the internal fields, i.e., the plastic flow relations (29) and (30), and the irreversibility condition (43). Therefore, we set

$$\tilde{\mathbf{q}} \in \tilde{\mathcal{Q}} := \tilde{\mathcal{U}} \times \tilde{\mathcal{B}} \times \cdots \times \tilde{\mathcal{B}} \times \tilde{\mathcal{K}}(\sqrt{\frac{2}{3}}\tilde{\boldsymbol{\varepsilon}}_1^p) \times \cdots \times \tilde{\mathcal{K}}(\sqrt{\frac{2}{3}}\tilde{\boldsymbol{\varepsilon}}_{n_y}^p) \times \tilde{\mathcal{R}}(\beta \sum_{s=1}^{n_y} \|\tilde{\boldsymbol{\varepsilon}}_s^p\|, \hat{\mathbf{n}}^g) \times \tilde{\mathcal{D}}. \quad (61)$$

The governing equations directly follow from enforcing the first order stability condition (19), the power balance (20) and the dissipation inequality (21). Exploiting the generality of the formulation presented in section 2.3, we directly replace the free energy density (44) and the dissipation potential (50) in the weak form of the first-order stability condition (22) to obtain, for all $\tilde{\mathbf{q}} \in \tilde{\mathcal{Q}}$:

$$\begin{aligned} & \int_{\Omega} \left[\sum_{s=1}^{n_y} \left((\boldsymbol{\sigma} - g(\alpha)H^{\text{kin}}\boldsymbol{\varepsilon}_s^p) : \hat{\mathbf{n}}_s - g(\alpha)\sqrt{\frac{2}{3}}(\boldsymbol{\sigma}_s^p + H_s^{\text{iso}}\boldsymbol{\kappa}_s) + \eta_p^2 \nabla \cdot \nabla \boldsymbol{\kappa}_s \right) \|\tilde{\boldsymbol{\varepsilon}}_s^p\| - \left(g'(\alpha)(\psi^{e+} + \psi^p) \right. \right. \\ & \left. \left. + g'(\alpha) \sum_{s=1}^{n_y} \sigma_s^p \boldsymbol{\kappa}_s + d(\gamma)(w'(\alpha) - \eta_d^2 \nabla \cdot d(\gamma)\nabla \alpha) \right) \tilde{\alpha} \right] d\mathbf{x} - \int_{\Gamma} \left(d(\gamma)\eta_d^2 \nabla \alpha \tilde{\alpha} + \eta_p^2 \sum_{s=1}^{n_y} \nabla \boldsymbol{\kappa}_s \tilde{\boldsymbol{\kappa}}_s \right) \cdot \mathbf{n} d\mathbf{x} \\ & \quad + \int_{\Omega} (\nabla \cdot \boldsymbol{\sigma} + \rho \mathbf{b}) \cdot \tilde{\mathbf{u}} d\mathbf{x} - \int_{\Gamma_N} (\boldsymbol{\sigma} \cdot \mathbf{n} - \bar{\mathbf{t}}) \cdot \tilde{\mathbf{u}} d\mathbf{x} \leq 0. \end{aligned} \quad (62)$$

Likewise, the power balance principle (23) gives

$$\begin{aligned} & \int_{\Omega} \left[\sum_{s=1}^{n_y} \left((\boldsymbol{\sigma} - g(\alpha)H^{\text{kin}}\boldsymbol{\varepsilon}_s^p) : \hat{\mathbf{n}}_s - g(\alpha)\sqrt{\frac{2}{3}}(\boldsymbol{\sigma}_s^p + H_s^{\text{iso}}\boldsymbol{\kappa}_s) + \eta_p^2 \nabla \cdot \nabla \boldsymbol{\kappa}_s \right) \|\dot{\boldsymbol{\varepsilon}}_s^p\| - \left(g'(\alpha)(\psi^{e+} + \psi^p) \right. \right. \\ & \left. \left. + g'(\alpha) \sum_{s=1}^{n_y} \sigma_s^p \boldsymbol{\kappa}_s + d(\gamma)(w'(\alpha) - \eta_d^2 \nabla \cdot d(\gamma)\nabla \alpha) \right) \dot{\alpha} \right] d\mathbf{x} - \int_{\Gamma} \left(d(\gamma)\eta_d^2 \nabla \alpha \dot{\alpha} + \eta_p^2 \sum_{s=1}^{n_y} \nabla \boldsymbol{\kappa}_s \dot{\boldsymbol{\kappa}}_s \right) \cdot \mathbf{n} d\mathbf{x} \\ & \quad + \int_{\Omega} (\nabla \cdot \boldsymbol{\sigma} + \rho \mathbf{b}) \cdot \dot{\mathbf{u}} d\mathbf{x} + \int_{\Gamma_N} (\boldsymbol{\sigma} \cdot \mathbf{n} - \bar{\mathbf{t}}) \cdot \dot{\mathbf{u}} d\mathbf{x} - \int_{\Gamma_D} (\boldsymbol{\sigma} \cdot \mathbf{n} - \mathbf{t}_r) \cdot \dot{\mathbf{u}} d\mathbf{x} = 0. \end{aligned} \quad (63)$$

As in section 2.3.2, Equations (62) and (63) yield the equilibrium equations and boundary conditions (1), along with equilibrium at the Dirichlet boundary. In turn, defining the s^{th} plastic yield function as

$$f_s^p := \|\boldsymbol{\sigma}_{\text{dev}} - g(\alpha)H^{\text{kin}}\boldsymbol{\varepsilon}_s^p\| - g(\alpha)\sqrt{\frac{2}{3}}(\sigma_s^p + H_s^{\text{iso}}\boldsymbol{\kappa}_s - \eta_p^2 \nabla \cdot \nabla \boldsymbol{\kappa}_s), \quad (64)$$

and the damage yield function as

$$f^d := -g'(\alpha)(\psi^{e+} + \psi^p) - g'(\alpha) \sum_{s=1}^{n_y} \sigma_s^p \boldsymbol{\kappa}_s - d(\gamma)w'(\alpha) + \eta_d^2 \nabla \cdot (d(\gamma)\nabla \alpha), \quad (65)$$

the evolution equations emerge from equations (62), (63) and the irreversibility condition (43) as loading/unloading systems, along with boundary conditions of the gradient-enhanced variables:

$$\begin{cases} f_s^p \leq 0, & f_s^p \dot{\boldsymbol{\kappa}}_s = 0, & \dot{\boldsymbol{\kappa}}_s \geq 0, & \left\{ f^d \leq 0, & f^d \dot{\alpha} = 0, & \dot{\alpha} \geq 0, \right. \\ \nabla \boldsymbol{\kappa}_s \cdot \mathbf{n} = 0, & \forall s \in Y, & & \left. \nabla \alpha \cdot \mathbf{n} = 0. \right. \end{cases} \quad (66)$$

3.4. An overview of the proposed model

Equation (64) can be viewed as a damage-dependent version of the purely plastic yield function (35). Specifically, the plastic driving force $\|\boldsymbol{\sigma}_{\text{dev}} - g(\alpha)H^{\text{kin}}\boldsymbol{\varepsilon}_s^{\text{p}}\|$ is now a function of damage through the stress tensor (48) and the back stress $g(\alpha)H^{\text{kin}}\boldsymbol{\varepsilon}_s^{\text{p}}$. Moreover, the size of the yield surface, interpreted as the plastic resisting force, is now given by

$$\sqrt{\frac{2}{3}}g(\alpha)(\boldsymbol{\sigma}_s^{\text{p}} + H_s^{\text{iso}}\boldsymbol{\kappa}_s + \eta_{\text{p}}^2\nabla \cdot \nabla\boldsymbol{\kappa}_s),$$

which progressively decreases as $\alpha \rightarrow 1$.

In the damage yield function (65), we identify

$$R(\alpha, \nabla\alpha, \gamma) := d(\gamma)w'(\alpha) - \eta_{\text{d}}^2\nabla \cdot d(\gamma)\nabla\alpha \quad (67)$$

as the damage resisting force with fatigue effects. We denote the damage driving force by $D := D^{\text{e}} + D^{\text{p}}$, where D^{e} and D^{p} are, respectively, elastic and plastic contributions given by

$$D^{\text{e}}(\boldsymbol{\varepsilon}^{\text{e}}, \alpha) := -g'(\alpha)\psi^{\text{e}+} \quad \text{and} \quad D^{\text{p}}(\boldsymbol{\varepsilon}^{\text{p}}, \boldsymbol{\kappa}, \nabla\boldsymbol{\kappa}, \alpha) := -g'(\alpha)\left(\psi^{\text{p}} + \sum_{s=1}^{n_{\text{y}}} \sigma_s^{\text{p}}\boldsymbol{\kappa}_s\right). \quad (68)$$

These definitions are useful to describe the mechanical response in the numerical simulations presented in section 4. Equation (65) can be written as

$$f^{\text{d}} = D(\boldsymbol{\varepsilon}^{\text{e}}, \boldsymbol{\varepsilon}^{\text{p}}, \boldsymbol{\kappa}, \nabla\boldsymbol{\kappa}, \alpha) - R(\alpha, \nabla\alpha, \gamma) = D^{\text{e}}(\boldsymbol{\varepsilon}^{\text{e}}, \alpha) + D^{\text{p}}(\boldsymbol{\varepsilon}^{\text{p}}, \boldsymbol{\kappa}, \nabla\boldsymbol{\kappa}, \alpha) - R(\alpha, \nabla\alpha, \gamma). \quad (69)$$

We observe in equation (69) two distinctive fatigue mechanisms:

1. The accumulation of elastic free energy, which, in the absence of plastic strains, drives cracks in the high-cycle fatigue regime. This effect is attained by the multiplicative degradation of the damage resisting force through $d(\gamma)$.
2. The accumulation of plastic energy (free and dissipated), which drives cracks in the low-cycle fatigue regime by additively increasing the damage driving force through D^{p} . This mechanism entails, on its own, a low-cycle fatigue process, that is accelerated when $d(\gamma) < 1$, where the plastic strains also contribute to the degradation of the damage resisting force (equation (55)). We associate the combination of $D^{\text{p}} > 0$ and $d(\gamma) < 1$ with very-low-cycle fatigue.

3.5. Incremental minimization and numerical implementation

As in section 2.4, consider the time discretization $0 = t_0 < \dots < t_n < t_{n+1} < \dots < t_{n_t} = t_{\text{max}}$, where all quantities are known up to t_n , and the goal is to find the state at the current time step t_{n+1} . For convenience, we introduce the following notations. A quantity \square evaluated at any previous time step $i \leq n$ is denoted as \square_i , while a quantity evaluated at t_{n+1} is written without a subscript, i.e., $\square := \square_{n+1}$. Moreover, the operator $\Delta\square := \square - \square_n$ is used to denote an increment from t_n to t_{n+1} .

The first step is to evaluate the incremental dissipated energy from the dissipation potential (50):

$$\begin{aligned}\mathcal{D}_{n+1} &= \mathcal{D}_n + \int_{\Omega} \int_{t_n}^{t_{n+1}} \left[\sum_{s=1}^{n_y} (g(\alpha)\sigma_s^p \dot{\kappa}_s + g'(\alpha)\sigma_s^p \kappa_s \dot{\alpha}) + \boldsymbol{\sigma} : \boldsymbol{\varepsilon}^r + d(\gamma)(w'(\alpha)\dot{\alpha} + \eta_d^2 \nabla \alpha \cdot \nabla \dot{\alpha}) \right] dt d\mathbf{x} \\ &= \mathcal{D}_n + \int_{\Omega} \int_{t_n}^{t_{n+1}} \left[\underbrace{\sum_{s=1}^{n_y} (g(\alpha)\sigma_s^p \dot{\kappa}_s + g'(\alpha)\sigma_s^p \kappa_s \dot{\alpha})}_{\text{path-independent}} + \underbrace{\boldsymbol{\sigma} : \boldsymbol{\varepsilon}^r + d(\gamma) \frac{d}{dt} \left(w(\alpha) + \frac{1}{2} \eta_d^2 \nabla \alpha \cdot \nabla \alpha \right)}_{\text{path-dependent}} \right] dt d\mathbf{x}.\end{aligned}\quad (70)$$

The integral of the path-independent part can be directly evaluated, while the path-dependent part is approximated according to section (2.4). As a result, equation (70) gives

$$\mathcal{D}_{n+1} = \mathcal{D}_n + \int_{\Omega} \left[\sum_{s=1}^{n_y} g(\alpha)\sigma_s^p \kappa_s + \boldsymbol{\sigma}_n : \Delta \boldsymbol{\varepsilon}^r + d(\gamma_n) \left(w(\alpha) + \frac{1}{2} \eta_d^2 \nabla \alpha \cdot \nabla \alpha - w(\alpha_n) - \frac{1}{2} \eta_d^2 \nabla \alpha_n \cdot \nabla \alpha_n \right) \right] d\mathbf{x}.\quad (71)$$

In view of equations (7), (9) and (44), a time-discrete energy functional is defined as

$$\Pi(\mathbf{u}, \boldsymbol{\varepsilon}^p, \boldsymbol{\kappa}, \boldsymbol{\varepsilon}^r, \alpha) = \mathcal{E}(\mathbf{u}, \boldsymbol{\varepsilon}^p, \boldsymbol{\kappa}, \boldsymbol{\varepsilon}^r, \alpha) - \mathcal{P}(\mathbf{u}) + \mathcal{D}_{n+1}.\quad (72)$$

The incremental minimization problem (27) takes the form

$$\inf_{\{\mathbf{u}, \boldsymbol{\varepsilon}^p, \boldsymbol{\kappa}, \boldsymbol{\varepsilon}^r, \alpha\} \in \mathcal{Q}} \{ \Pi(\mathbf{u}, \boldsymbol{\varepsilon}^p, \boldsymbol{\kappa}, \boldsymbol{\varepsilon}^r, \alpha) \mid \Delta \kappa_s = \sqrt{\frac{2}{3}} \|\Delta \boldsymbol{\varepsilon}_s^p\| \forall s \in Y, \Delta \boldsymbol{\varepsilon}^r = \beta \hat{\mathbf{n}}_n^g \sum_{s=1}^{n_y} \|\Delta \boldsymbol{\varepsilon}_s^p\|, \Delta \alpha \geq 0 \},\quad (73)$$

where we impose irreversibility and the incremental counterparts of the plastic flow relations (29) and (30).

The numerical solution of the variational problem (73) is based on an extension of the alternate minimization algorithm [90] to ductile fracture [31, 38], which exploits the fact that while the functional (72) is non-convex, it is convex with respect to each primary field individually. In this setting, we seek the solution of a sequence of convex optimization problems, aiming to iteratively converge to a stationary state. The procedure is summarized in algorithm 1, along with the equations presented below.

Given \mathbf{q}_i for all $i \in \{1, \dots, n\}$, we solve, alternatively, the following coupled sub-problems.

Minimization with respect to the displacement field. Given $\{\boldsymbol{\varepsilon}^p, \boldsymbol{\kappa}, \boldsymbol{\varepsilon}^r, \alpha\}$, find

$$\mathbf{u} = \arg \inf_{\mathbf{u} \in \mathcal{U}} \{ \Pi(\mathbf{u}, \boldsymbol{\varepsilon}^p, \boldsymbol{\kappa}, \boldsymbol{\varepsilon}^r, \alpha) \}\quad (74)$$

from the necessary condition

$$\int_{\Omega} (\boldsymbol{\sigma} : \nabla^s \tilde{\mathbf{u}} - \rho \mathbf{b} \cdot \tilde{\mathbf{u}}) dx - \int_{\Gamma_N} \bar{\mathbf{t}} \cdot \tilde{\mathbf{u}} dx = 0 \quad \forall \tilde{\mathbf{u}} \in \tilde{\mathcal{U}}.\quad (75)$$

Given that $\mathbf{u} \in \mathcal{U}$, this problem constitutes the weak form of the equilibrium equations (1).

Minimization with respect to the plastic fields. Given $\{\mathbf{u}, \alpha\}$, find

$$\begin{aligned}\{\boldsymbol{\varepsilon}^p, \boldsymbol{\kappa}, \boldsymbol{\varepsilon}^r\} &= \arg \inf_{\{\boldsymbol{\varepsilon}^p, \boldsymbol{\kappa}, \boldsymbol{\varepsilon}^r\} \in \mathcal{P}} \{ \Pi(\mathbf{u}, \boldsymbol{\varepsilon}^p, \boldsymbol{\kappa}, \boldsymbol{\varepsilon}^r, \alpha) \} \\ \text{s.t.} \quad \Delta \kappa_s &= \sqrt{\frac{2}{3}} \|\Delta \boldsymbol{\varepsilon}_s^p\| \forall s \in Y, \Delta \boldsymbol{\varepsilon}^r = \beta \hat{\mathbf{n}}_n^g \sum_{s=1}^{n_y} \|\Delta \boldsymbol{\varepsilon}_s^p\|.\end{aligned}\quad (76)$$

Algorithm 1 Alternate minimization.

Input: $\mathbf{q}_i \in \mathcal{Q}$ for all $i = 1, \dots, n$.

Output: $\mathbf{q}_{n+1} \in \mathcal{Q}$.

1: Initialize iterations $j = 0$ and set $\{\boldsymbol{\varepsilon}^{\text{P}(0)}, \boldsymbol{\kappa}^{(0)}, \boldsymbol{\varepsilon}^{\text{r}(0)}, \alpha^{(0)}\} := \{\boldsymbol{\varepsilon}_n^{\text{P}}, \boldsymbol{\kappa}_n, \boldsymbol{\varepsilon}_n^{\text{r}}, \alpha_n\}$.

2: **repeat**

3: Set $j \leftarrow j + 1$.

4: Find

$$\mathbf{u}^{(j)} := \arg \inf_{\mathbf{u} \in \mathcal{U}} \Pi(\mathbf{u}, \boldsymbol{\varepsilon}^{\text{P}(j-1)}, \boldsymbol{\kappa}^{(j-1)}, \boldsymbol{\varepsilon}^{\text{r}(j-1)}, \alpha^{(j-1)})$$

from equation (75).

5: Find

$$\begin{aligned} \{\boldsymbol{\varepsilon}^{\text{P}(j)}, \boldsymbol{\kappa}^{(j)}, \boldsymbol{\varepsilon}^{\text{r}(j)}\} &:= \arg \inf_{\{\boldsymbol{\varepsilon}^{\text{P}}, \boldsymbol{\kappa}, \boldsymbol{\varepsilon}^{\text{r}}\} \in \mathcal{D}} \left\{ \Pi(\mathbf{u}^{(j)}, \boldsymbol{\varepsilon}^{\text{P}}, \boldsymbol{\kappa}, \boldsymbol{\varepsilon}^{\text{r}}, \alpha^{(j-1)}) + \int_{\Omega} \sum_{s=1}^{n_y} I_+(\Delta \kappa_s) \, d\mathbf{x} \right\} \\ \text{s.t. } \Delta \boldsymbol{\varepsilon}_s^{\text{P}} &= \sqrt{\frac{3}{2}} \hat{\mathbf{n}}_s^{\text{tr}} \Delta \kappa_s \quad \forall s \in Y, \quad \Delta \boldsymbol{\varepsilon}^{\text{r}} = \sqrt{\frac{3}{2}} \beta \hat{\mathbf{n}}_n^{\text{g}} \sum_{s=1}^{n_y} \Delta \kappa_s \end{aligned}$$

from equation (78).

6: Find

$$\alpha^{(j)} = \arg \inf_{\alpha \in \mathcal{D}} \Pi(\mathbf{u}^{(j)}, \boldsymbol{\varepsilon}^{\text{P}(j)}, \boldsymbol{\kappa}^{(j)}, \boldsymbol{\varepsilon}^{\text{r}(j)}, \alpha)$$

from equation (80).

7: **until** $\|\mathbf{u}^j - \mathbf{u}^{j-1}\|$, $\|\boldsymbol{\kappa}^j - \boldsymbol{\kappa}^{j-1}\|$ and $\|\alpha^j - \alpha^{j-1}\|$ are sufficiently small.

8: Set $\mathbf{q}_{n+1} := \mathbf{q}^{(j)}$.

Since the solution of this problem is not straightforward, we make use of the concepts discussed in section 3.1 to formulate a reduced problem in terms of the scalar field κ_s . In view of (29), $\Delta \kappa_s = \sqrt{2/3} \|\Delta \boldsymbol{\varepsilon}_s^{\text{P}}\|$, which, from standard arguments of J_2 plasticity, implies

$$\Delta \boldsymbol{\varepsilon}_s^{\text{P}} = \sqrt{\frac{3}{2}} \hat{\mathbf{n}}_s^{\text{tr}} \Delta \kappa_s, \quad \text{with} \quad \hat{\mathbf{n}}_s^{\text{tr}} = \frac{\boldsymbol{\varsigma}_{\text{sdev}}^{\text{ptr}}}{\|\boldsymbol{\varsigma}_{\text{sdev}}^{\text{ptr}}\|} \equiv \hat{\mathbf{n}}_s \quad \text{and} \quad \boldsymbol{\varsigma}_{\text{sdev}}^{\text{ptr}} := \boldsymbol{\sigma}_{\text{dev}}(\boldsymbol{\varepsilon}, \boldsymbol{\varepsilon}_n^{\text{P}}, \boldsymbol{\varepsilon}_n^{\text{r}}, \alpha) - H_s^{\text{kin}} \boldsymbol{\varepsilon}_{sn}^{\text{P}}.$$

The minimization problem (76) is then rewritten as

$$\begin{aligned} \{\boldsymbol{\varepsilon}^{\text{P}}, \boldsymbol{\kappa}, \boldsymbol{\varepsilon}^{\text{r}}\} &= \arg \inf_{\{\boldsymbol{\varepsilon}^{\text{P}}, \boldsymbol{\kappa}, \boldsymbol{\varepsilon}^{\text{r}}\} \in \mathcal{D}} \left\{ \Pi(\mathbf{u}, \boldsymbol{\varepsilon}^{\text{P}}, \boldsymbol{\kappa}, \boldsymbol{\varepsilon}^{\text{r}}, \alpha) + \int_{\Omega} \sum_{s=1}^{n_y} I_+(\Delta \kappa_s) \, d\mathbf{x} \right\} \\ \text{s.t. } \Delta \boldsymbol{\varepsilon}_s^{\text{P}} &= \sqrt{\frac{3}{2}} \hat{\mathbf{n}}_s^{\text{tr}} \Delta \kappa_s \quad \forall s \in Y, \quad \Delta \boldsymbol{\varepsilon}^{\text{r}} = \sqrt{\frac{3}{2}} \beta \hat{\mathbf{n}}_n^{\text{g}} \sum_{s=1}^{n_y} \Delta \kappa_s, \end{aligned} \tag{77}$$

where the indicator function $I_+ : \mathbb{R} \rightarrow \mathbb{R} \cup \{+\infty\}$ is used to impose irreversibility on κ_s . Replacing the space of virtual ratcheting strains $\tilde{\mathcal{H}}(\cdot, \hat{\mathbf{n}}^{\text{g}})$ by its incremental approximation $\tilde{\mathcal{H}}(\cdot, \hat{\mathbf{n}}_n^{\text{g}})$, the necessary condition

for (77) reads, for all $\{\tilde{\boldsymbol{\varepsilon}}_s^p, \tilde{\kappa}_s, \tilde{\boldsymbol{\varepsilon}}^r\} \in \tilde{\mathcal{B}} \times \tilde{\mathcal{H}}(\sqrt{\frac{2}{3}}\tilde{\boldsymbol{\varepsilon}}_s^p) \times \tilde{\mathcal{H}}(\beta \sum_{s=1}^{n_y} \|\tilde{\boldsymbol{\varepsilon}}_s^p\|, \hat{\mathbf{n}}_n^g)$:

$$\int_{\Omega} \left[\left(\sqrt{\frac{3}{2}} \|\boldsymbol{\sigma}_{\text{dev}} - g(\alpha) H^{\text{kin}} \boldsymbol{\varepsilon}_s^p\| - g(\alpha) (\boldsymbol{\sigma}_s^p + H_s^{\text{iso}} \kappa_s) \right. \right. \\ \left. \left. + \sqrt{\frac{3}{2}} \beta \Delta \boldsymbol{\sigma} : \hat{\mathbf{n}}_n^g - \partial_{\kappa_s} I_+(\Delta \kappa_s) \right) \tilde{\kappa}_s - \eta_p^2 \nabla \kappa_s \cdot \nabla \tilde{\kappa}_s \right] d\mathbf{x} = 0, \quad \forall s \in Y, \quad (78)$$

with $\boldsymbol{\varepsilon}_s^p = \boldsymbol{\varepsilon}_{sn}^p + \sqrt{\frac{3}{2}} \hat{\mathbf{n}}_s^{\text{tr}} \Delta \kappa_s$ and $\boldsymbol{\varepsilon}^r = \boldsymbol{\varepsilon}_n^r + \sqrt{\frac{3}{2}} \beta \hat{\mathbf{n}}_n^g \sum_{s=1}^{n_y} \Delta \kappa_s$.

In view of the multivalued function $\partial_{\kappa_s} I_+(\Delta \kappa_s)$, equation (78) approximates, in weak form, the plastic loading/unloading conditions in equation (66) at t_{n+1} , where the exact equations are recovered by letting the term $\beta \Delta \boldsymbol{\sigma} : \hat{\mathbf{n}}_n^g$ vanish for small-enough time steps. Note that equation (78) constitutes a system of n_y equations with coupled κ_s for all $s \in Y$. This system can be solved iteratively, for instance, using a fixed-point iteration scheme.

Minimization with respect to the damage field. Given $\{\mathbf{u}, \boldsymbol{\varepsilon}^p, \boldsymbol{\kappa}, \boldsymbol{\varepsilon}^r\}$, find

$$\alpha = \arg \inf_{\alpha \in \mathcal{D}} \{ \Pi(\mathbf{u}, \boldsymbol{\varepsilon}^p, \boldsymbol{\kappa}, \boldsymbol{\varepsilon}^r, \alpha) + \int_{\Omega} I_+(\Delta \alpha) d\mathbf{x} \}, \quad (79)$$

where, as in (77), the indicator function is used to impose irreversibility. Equation (79) yields, for all $\tilde{\alpha} \in \mathcal{D}$, the necessary condition

$$\int_{\Omega} \left[\left(-g'(\alpha) (\psi^{e+} + \psi^p) - g'(\alpha) \sum_{s=1}^{n_y} \sigma_s^p \kappa_s - d(\gamma_n) w'(\alpha) - \partial_{\alpha} I_+(\Delta \alpha) \right) \tilde{\alpha} - d(\gamma_n) \eta_d^2 \nabla \alpha \cdot \nabla \tilde{\alpha} \right] d\mathbf{x} = 0, \quad (80)$$

which recovers the damage loading/unloading conditions in equation (66).

Equations (75), (78) and (80) are suitable for spatial discretization using standard finite elements. Moreover, the plastic and damage equations (78) and (80) can be solved using techniques for PDE-constrained optimization to account for irreversibility and the box constraint $\alpha \in [0, 1]$ in Ω . Examples of such techniques in the context of phase-field fracture modeling are outlined by Gerasimov and De Lorenzis [91].

4. Numerical simulations

This section presents numerical simulations that highlight the main features of the model described in section 3. First, we study the undamaged behavior of the cyclic plasticity model in a 2D problem. This example allows to describe a variety of plastic responses with cyclic effects under force control and displacement control. We then study the results of the plastic-damage coupling with fatigue effects. In order to highlight the fatigue mechanisms and their interplay, the homogeneous uniaxial response is first studied. Then, a 2D simulation is presented, which describes the initiation and propagation of ductile fatigue cracks.

4.1. Plastic response: perforated specimen

This example consists of a square specimen with a central hole under plane strain conditions and cyclic loading, alternatively subjected to force control and displacement control. Due to symmetry conditions, only the top-right quarter of the specimen is analyzed (figure 1), and uniform loading is applied on the top border.

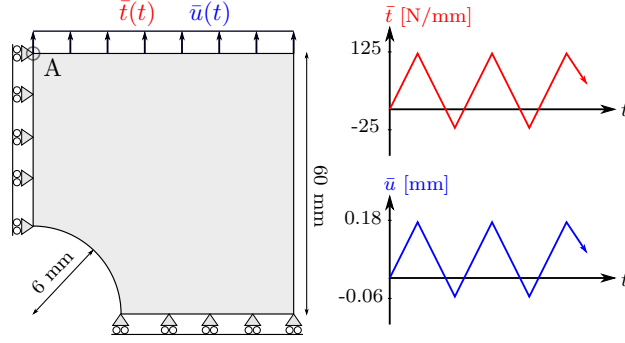


Fig. 1. Schematic representation of the perforated specimen under force control and displacement control.

Damage is disallowed by setting, in the general model, a sufficiently large damage threshold w_0 . The plastic evolution is modeled using a single yield surface ($n_y = 1$), and we consider a Young's modulus $E = 205 \times 10^3$ MPa, a Poisson's ratio $\nu = 0.3$, a plastic yield strength $\sigma_1^p = 100$ MPa and a plastic internal length $\eta_p = 0.6$ N^{1/2}. The remaining parameters vary according to table 1, where the kinematic hardening modulus is combined with a positive (negative) isotropic hardening modulus to describe cyclic hardening (softening). Moreover, ratcheting and stress relaxation effects are attained by choosing $\beta > 0$.

Table 1. Varying parameters for the cyclically plastic responses of the perforated specimen.

Load control	Response	H_1^{kin} [MPa]	H_1^{iso} [MPa]	β [-]
Force	KH	22777.78	0	0
	KH-IH	22550.00	227.78	0
	KH-IS	22686.67	-91.11	0
	KH-R	22777.78	0	0.4
	KH-IH-R	22550.00	227.78	0.4
	KH-IS-R	22686.67	-91.11	0.4
Displacement	KH	22777.78	0	0
	KH-IH	22759.56	18.22	0
	KH-IS	22759.56	-18.22	0
	KH-R	22777.78	0	0.4
	KH-IH-R	22759.56	18.22	0.8
	KH-IS-R	22759.56	-18.22	0.8

Figure 2 shows the cyclic responses under force control, corresponding to the force-displacement curves in the vertical direction at location A due to a uniform distributed force of magnitude $\bar{t}(t)$ (figure 1). The kinematic hardening response (KH, figure 2a) exhibits closed hysteretic cycles, capturing the Bauschinger effect. The incorporation of isotropic hardening (KH-IH, figure 2b) results in a progressive decrease of

cyclic displacements, leading to a closed plastic loop. The opposite occurs with isotropic softening (KH-IS, figure 2c), where the cyclic displacements progressively increase as the size of the yield surface decreases. The combination of these responses with ratcheting effects results in more complex cyclic evolutions. Kinematic hardening and ratcheting (KH-R, figure 2d) exhibits ratcheting (mean cyclic displacement increments) at a constant rate. Combining ratcheting with isotropic hardening (KH-IH-R, figure 2e) results in a competition between both mechanisms, where the ratcheting effect tends to vanish as the equivalent plastic strains increase. As a result of the loading pattern, this response occurs asymmetrically, with more pronounced cyclic hardening during tensile loading. Finally, the combination of kinematic hardening, isotropic softening and ratcheting (KH-IS-R, figure 2f) leads to an asymmetric, accelerated ratcheting response. Figure 3 shows the equivalent plastic strains at different load cycles for KH-IS-R, while the contour plots for the other responses are not shown due to their qualitative similarity. The plastic strains localize near the hole with an inclined spatial distribution, where the non-local effect governed by the plastic length scale allows to control the characteristic size of the localization region.

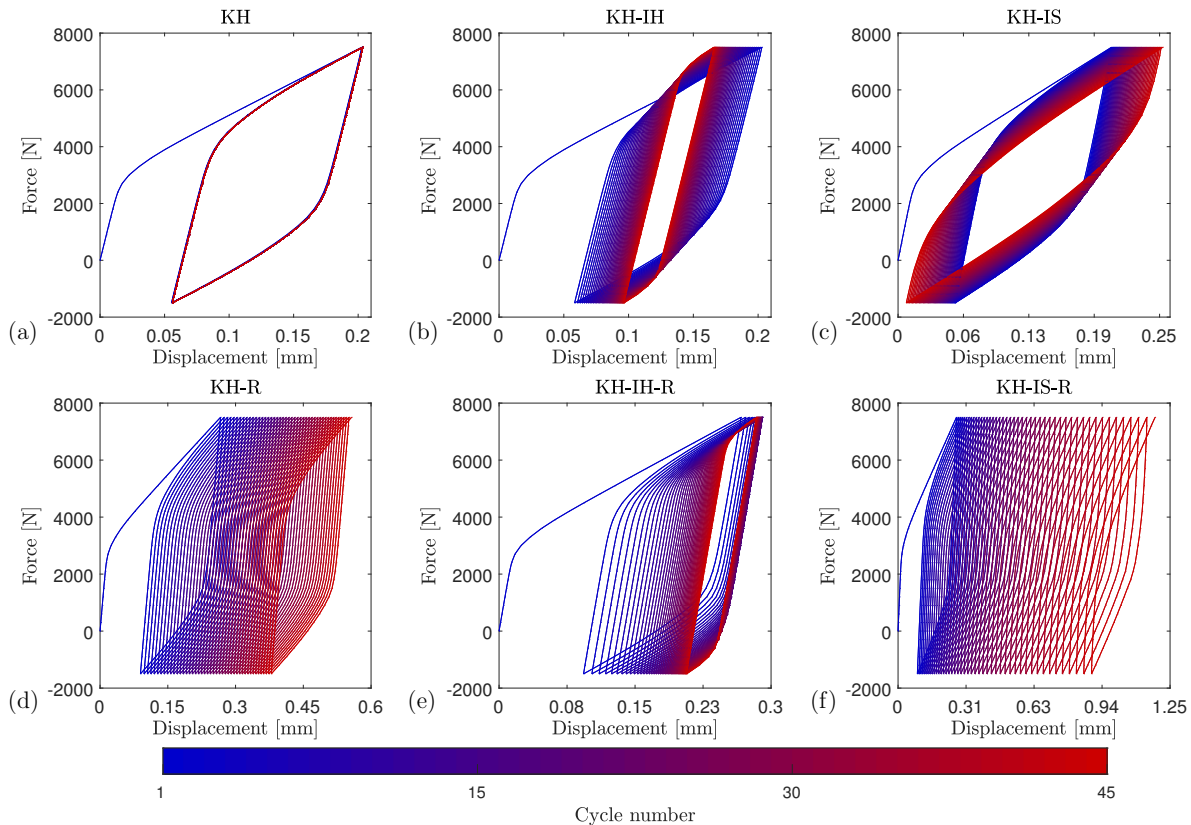


Fig. 2. Force-displacement curves measured at location A of the perforated specimen under force control (figure 1), showing the cyclic response with (a) KH, (b) KH-IH, (c) KH-IS, (d) KH-R, (e) KH-IH-R and (f) KH-IS-R.

Figure 4 shows the cyclic responses under displacement-control cycles of magnitude $\bar{u}(t)$ applied on the top border (figure 1). As in force control, a closed cycle is observed for KH (figure 4a), while the yield surface

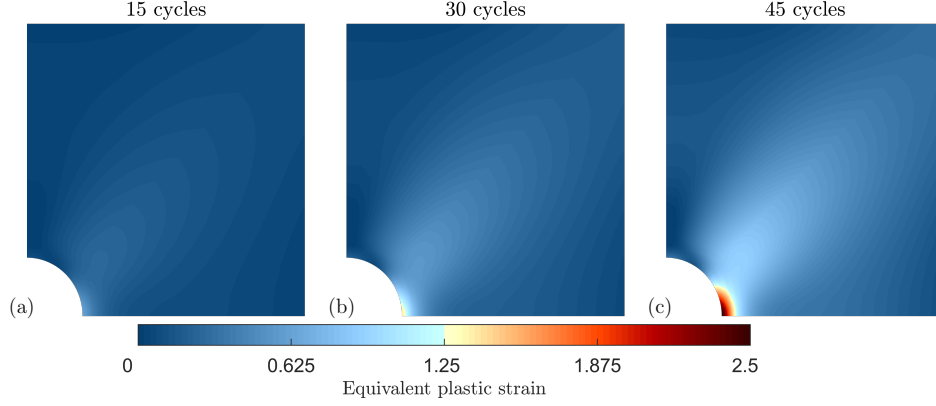


Fig. 3. Equivalent plastic strain for the KH-IS-R response of the perforated specimen under force control after (a) 15, (b) 30 and (c) 45 cycles.

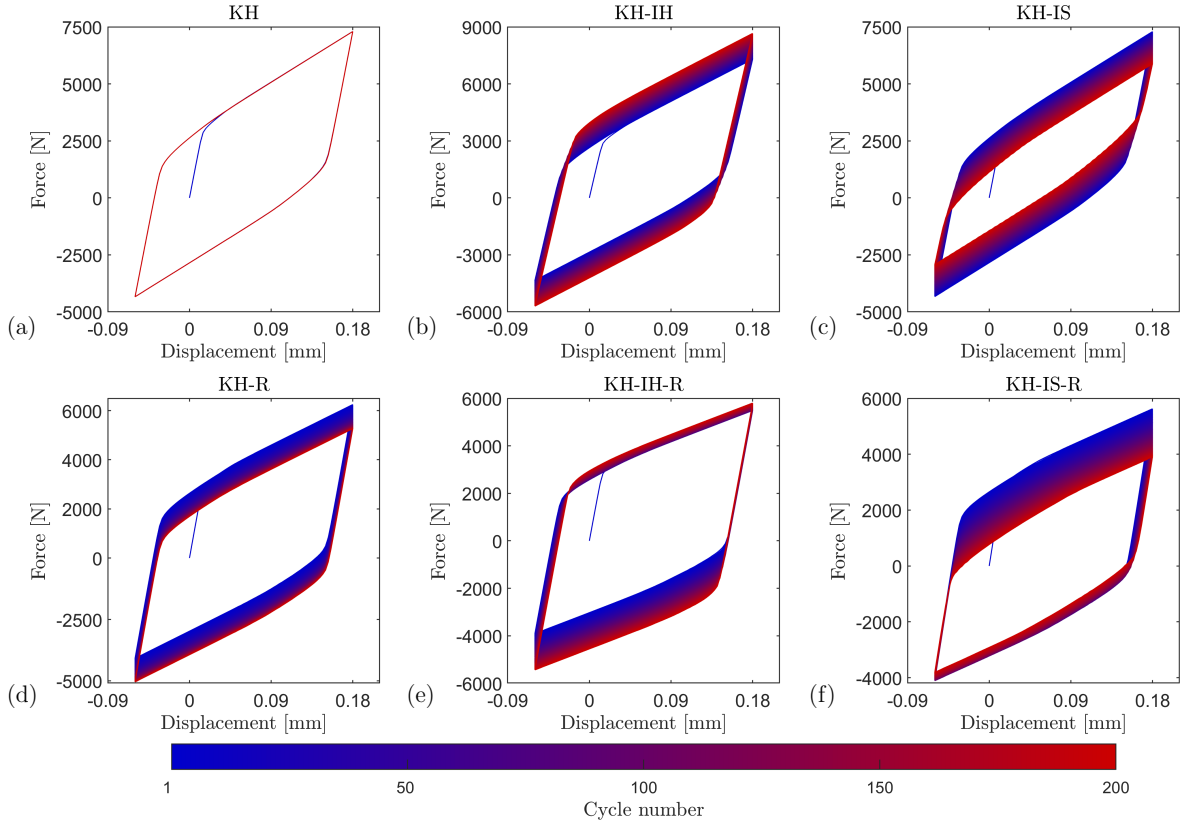


Fig. 4. Force-displacement curves measured at the top border of the perforated specimen under displacement control (figure 1), showing the cyclic response with (a) KH, (b) KH-IH, (c) KH-IS, (d) KH-R, (e) KH-IH-R and (f) KH-IS-R.

progressively grows for KH-IH (figure 4b), leading to an elastic response after a sufficiently large number of cycles. The opposite occurs for KH-IS (figure 4c), where the size of the yield surface progressively vanishes. In both KH-IH and KH-IS, the response is symmetric in tension and compression. However, for $\beta > 0$ (non-zero ratcheting strains), the response becomes asymmetric. This interesting effect of the ratcheting model

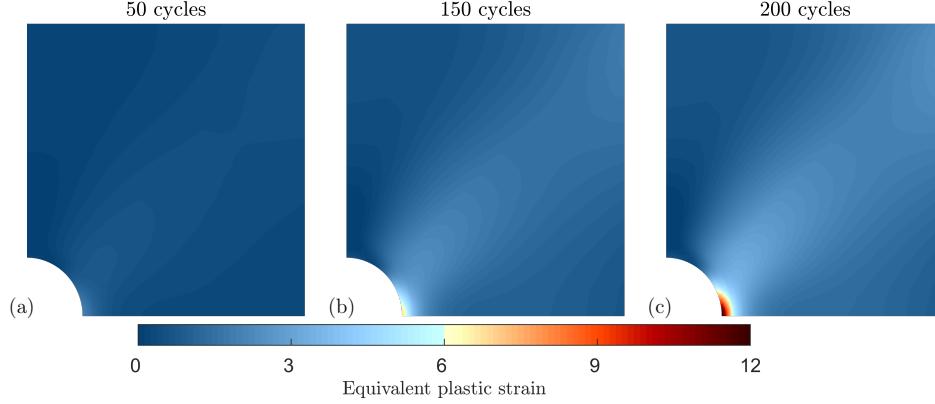


Fig. 5. Equivalent plastic strain for the KH-IS-R response of the perforated specimen under displacement control after a) 50, b) 150 and c) 200 cycles.

allows to capture stress relaxation, as shown in figure 4d for KH-R, where the plastic cycles shift downwards and stabilize in a closed loop that corresponds to zero mean stresses. Moreover, a pronounced asymmetrical response is observed for both KH-IH-R (figure 4e) and KH-IS-R (figure 4f), which combine stress relaxation with cyclic hardening and cyclic softening, respectively. Figure 5 shows the equivalent plastic strains at different load cycles for KH-IS-R, which qualitatively resemble the results obtained under force control.

4.2. Coupled plastic-damage response

4.2.1. Homogeneous uniaxial test

The aim of this example is to provide an interpretation of the failure mechanisms that result from coupling cyclic plasticity to damage with fatigue effects. For illustrative purposes, we study the response of a single 1D element under force control and displacement control. To this end, the multidimensional model presented in section 3 is reduced to the 1D case, where all vector- and tensor-valued quantities are replaced by scalar quantities. In addition, the factor $\sqrt{3/2}$ is dropped from equation (29) and everything that follows, and the energy split from equation (47) is no longer considered.

Table 2. Fixed parameters for the coupled homogeneous responses, with varying parameters shown in table 3. σ_s^p and H_s^{kin} vary linearly from $s = 1$ to $s = n_y$, with $n_y = 20$ for force control and $n_y = 10$ for displacement control.

Load control	Model	E	w_0	γ_0	k	n_y	σ_1^p	$\sigma_{n_y}^p$	H_1^{kin}	$H_{n_y}^{\text{kin}}$
		[MPa]	[MPa]	[MPa]	[-]	[-]	[MPa]	[MPa]	[MPa]	[MPa]
Force	AT-2	10	260	10	0.4	20	0.6	1.4	100	9.09
Displacement	AT-1	1	350	10	0.7	10	0.4	0.7	8	0.73

To capture a smooth stress-strain response, the 1D element is modeled with multi-surface plasticity ($n_y > 1$). Moreover, the parameters shown in tables 2 and 3 are selected such that the various responses that emerge from the cyclic plasticity model are affected by damage evolution.

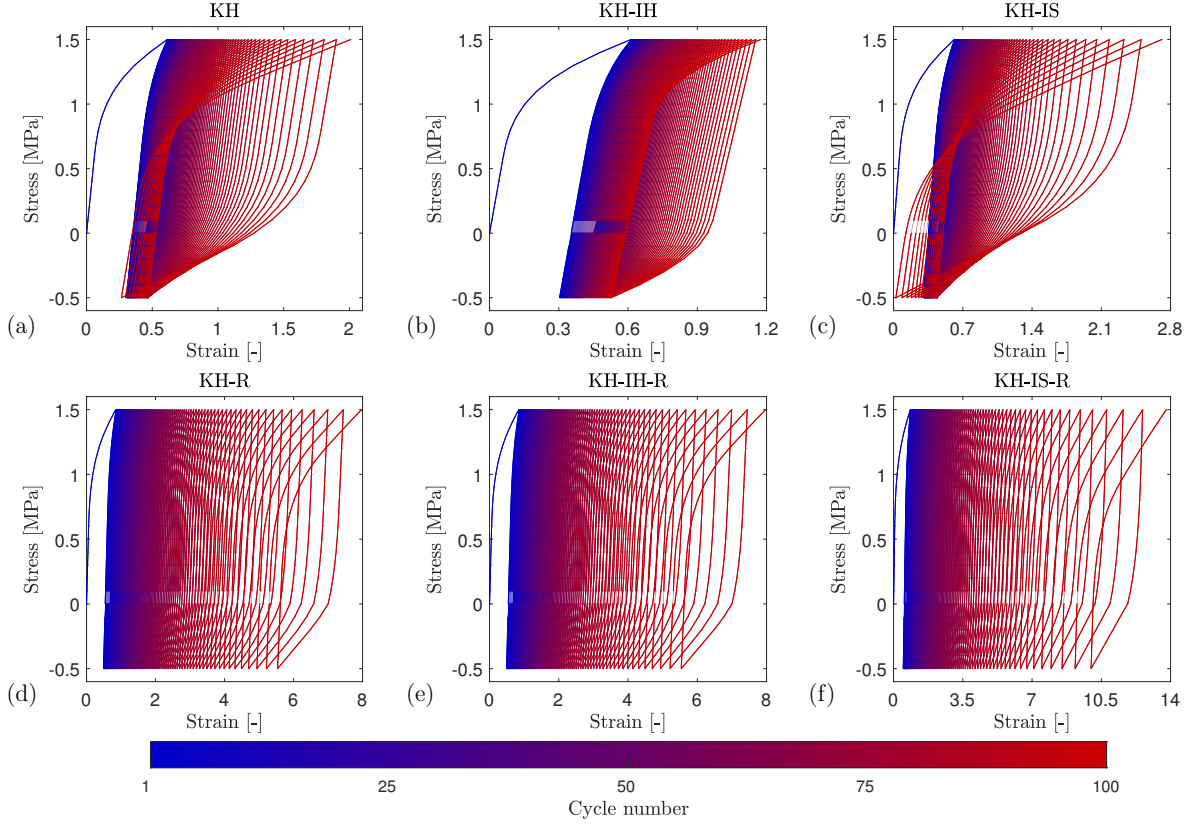


Fig. 6. Stress-strain curves of the homogeneous uniaxial tests under force control, showing (a) KH, (b) KH-IH, (c) KH-IS, (d) KH-R, (e) KH-IH-R and (f) KH-IS-R coupled to damage with fatigue effects.

Figure 6 shows the responses under force control, corresponding to imposed stress cycles between -0.5 MPa and 1.5 MPa. The initial plastic responses resemble the results in figure 2. However, as damage evolves, cyclic softening is triggered in all cases. Therefore, the softening responses are accelerated, while the (initially) hardening responses shift to a cyclic softening regime. An analogous result is observed in figure 7 for the case of displacement control, corresponding to imposed strain cycles between magnitudes of -1 and 2 .

As discussed previously, the coupled plastic-damage model includes a fatigue mechanism that degrades the damage resisting force through $d(\gamma)$ as a function of free energy accumulation. Thus, in the absence of plastic strains, damage is accelerated for the AT-2 model and triggered after an initial elastic response for the AT-1 model, leading to a high-cycle fatigue process. Responses of this type are thoroughly studied in references [12] and [13]. On the other hand, the accumulation of plastic strains leads, on its own, to a plastic fatigue mechanism that promotes damage evolution through the plastic driving force D^p . We associate this process with low-cycle fatigue, and the combination of D^p and $d(\gamma)$ with very-low-cycle fatigue.

The fatigue mechanisms and their interplay are analyzed in figures 8 to 11 for KH-IS-R. Figure 8 shows the mechanical response for the force control test with the parameters from tables 2 and 3, but setting $\gamma_0 = \infty$, such that damage is only driven by the accumulation of plastic strains. The ratcheting strain ε^r

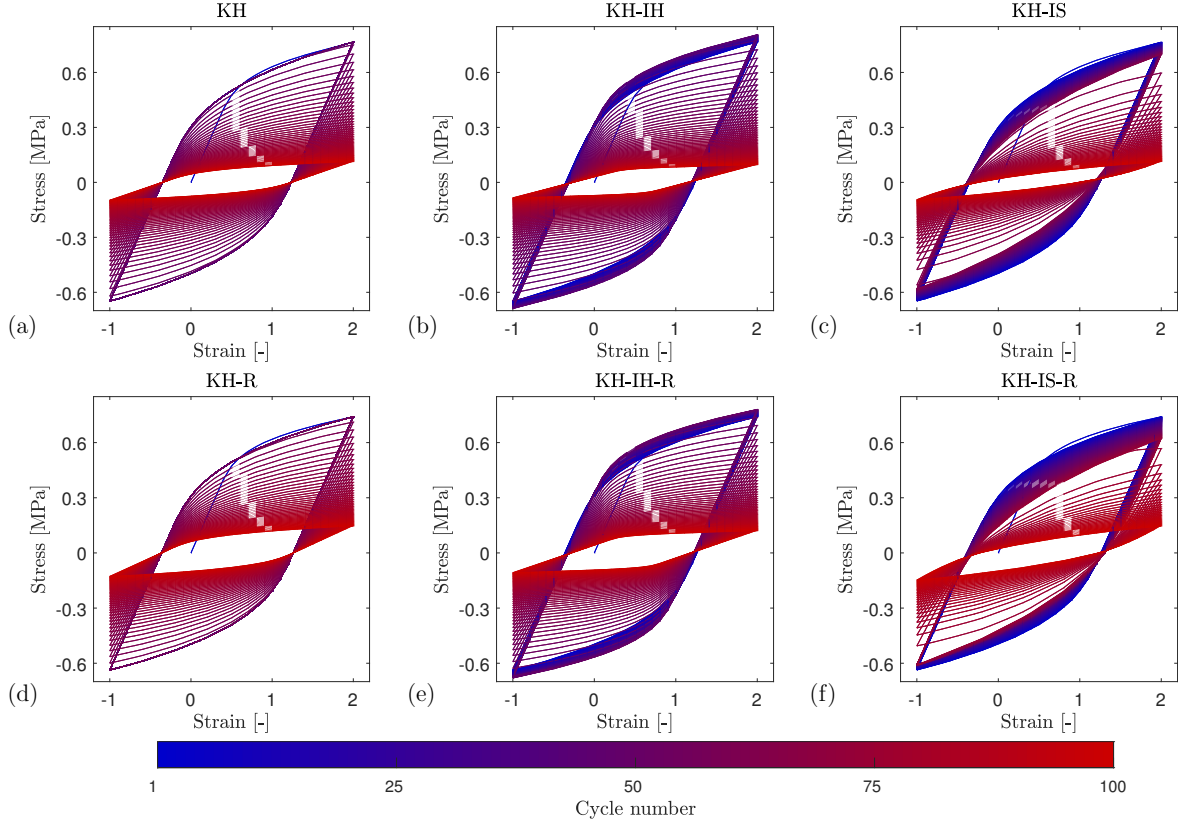


Fig. 7. Stress-strain curves of the homogeneous uniaxial tests under displacement control, showing (a) KH, (b) KH-IH, (c) KH-IS, (d) KH-R, (e) KH-IH-R and (f) KH-IS-R coupled to damage with fatigue effects.

grows in an accelerated manner, where the mean cyclic value progressively increases, while the plastic strains ε_s^p grow in amplitude. These responses are reflected in the cyclic evolution of the total strain ε (figure 8b). As a result of the AT-2 model, the damage resisting force $R = 2w_0\alpha$ grows as damage evolves. This occurs at every loading stage, where the resisting force intersects the total driving force D (figure 8d). Figure 9 shows the counterpart simulation with $\gamma_0 = 10$ MPa. The ratcheting strain, the total strain and the plastic strains present the same evolution pattern, but grow at a notably higher rate (figure 9a). This is a consequence of the accelerated growth of the damage variable that occurs as $d(\gamma)$ decreases (figure 9c). This response results from the combined effect of D^p and $d(\gamma)$, where the fatigue variable γ is driven by the sum of elastic free energy and plastic free energy.

For the case of displacement control (figures 10 and 11), we change the parameters from table 2 to $w_0 = 30$ MPa, $H_1^{\text{iso}} = -0.08$ MPa and $H_{n_y}^{\text{iso}} = -0.0073$ MPa, to accelerate the damage evolution for illustrative purposes. We then set, alternatively, $\gamma_0 = \infty$ and $\gamma_0 = 1$ MPa. Figure 10 shows the mechanical response of the displacement control test with $\gamma_0 = \infty$, where we observe a relatively slow stress decay (figure 10b). As a result of the AT-1 model, damage is triggered after 11 cycles (figure 10c). This occurs when the total driving force D , modulated by the plastic driving force D^p , intersects the constant-valued

Table 3. Varying parameters for the coupled homogeneous responses, with fixed parameters shown in table 2. H_s^{kin} varies linearly from $s = 1$ to $s = n_y$, with $n_y = 20$ for force control and $n_y = 10$ for displacement control.

Load control	Response	H_1^{iso} [MPa]	$H_{n_y}^{\text{iso}}$ [MPa]	β [-]
Force	KH	0	0	0
	KH-IH	0.2	0.0182	0
	KH-IS	-0.08	-0.0073	0
	KH-R	0	0	0.5
	KH-IH-R	0.2	0.0182	0.5
	KH-IS-R	-0.08	-0.0073	0.5
Displacement	KH	0	0	0
	KH-IH	0.02	0.0018	0
	KH-IS	-0.018	-0.0016	0
	KH-R	0	0	0.2
	KH-IH-R	0.02	0.0018	0.2
	KH-IS-R	-0.018	-0.0016	0.2

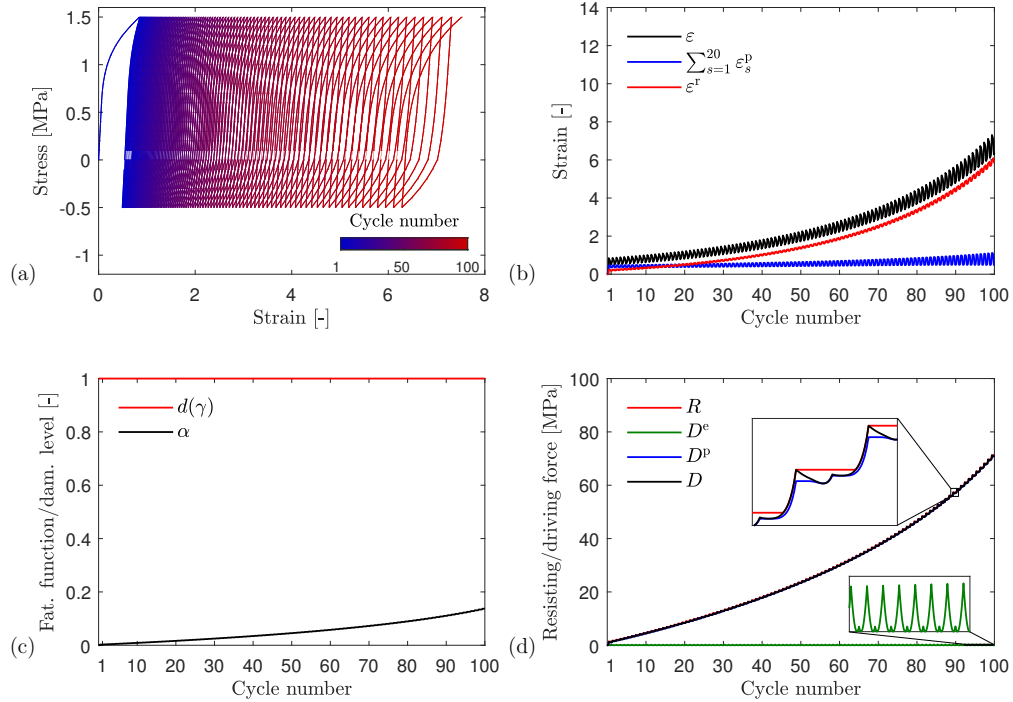


Fig. 8. KH-IS-R homogeneous response with damage ($\gamma_0 = \infty$) under force control: (a) stress-strain curve and corresponding time histories for the (b) strains, (c) damage and fatigue degradation and (d) damage driving and resisting forces.

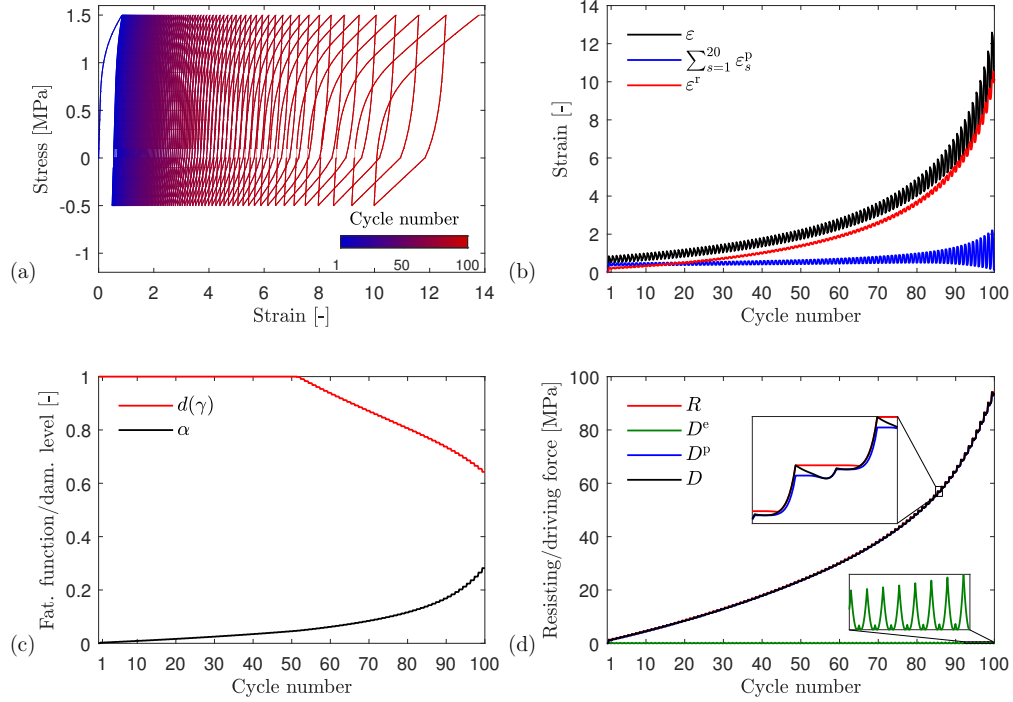


Fig. 9. KH-IS-R homogeneous response with damage ($\gamma_0 = 10$ MPa) under force control: (a) stress-strain curve and corresponding time histories for the (b) strains, (c) damage and fatigue degradation and (d) damage driving and resisting forces.

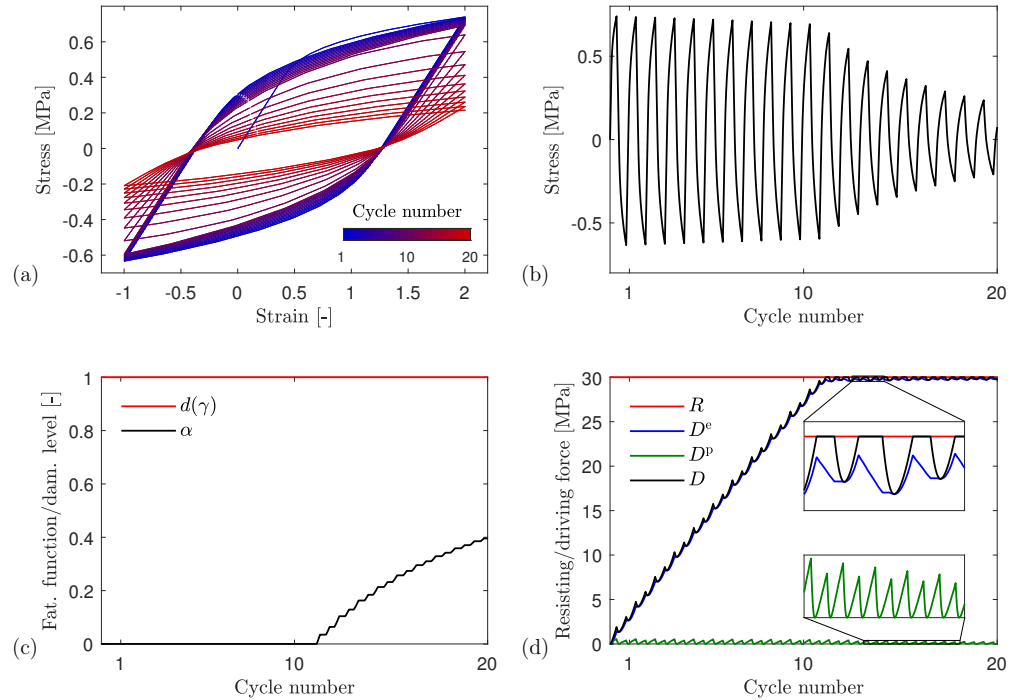


Fig. 10. KH-IS-R homogeneous response with damage ($\gamma_0 = \infty$) under displacement control: (a) stress-strain curve and corresponding time histories for the (b) stress, (c) damage and fatigue degradation and (d) damage driving and resisting forces.

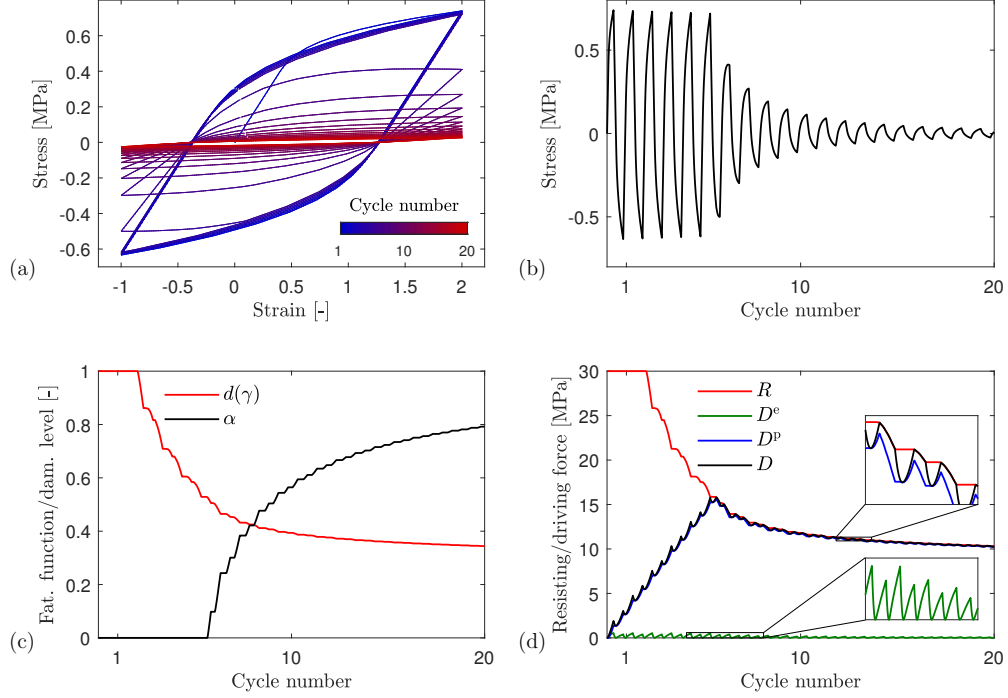


Fig. 11. KH-IS-R homogeneous response with damage ($\gamma_0 = 1$ MPa) under displacement control: (a) stress-strain curve and corresponding time histories for the (b) stress, (c) damage and fatigue degradation and (d) damage driving and resisting forces.

resisting force R (figure 10d). Figure 11 shows the counterpart with $\gamma_0 = 1$ MPa, where the resisting force begins to decrease after 2 cycles, causing damage to be triggered after only 5 cycles (figures 11c and 11d). Consequently, figure 11b shows a notably faster stress decay than figure 10b, as expected in very-low-cycle fatigue.

4.2.2. Asymmetrically notched specimen

This example aims to describe the initiation, growth and merging of ductile cracks in a low-cycle fatigue process, driven by the accumulation and localization of isochoric plastic deformations. For this purpose, we subject an asymmetrically notched specimen in plane strain conditions to displacement cycles, as schematically shown in figure 12, where the bottom border is fixed and vertical displacements of magnitude $\bar{u}(t)$ are imposed on the top border. We describe the plastic response with a single yield surface ($n_y = 1$) and kinematic hardening, where failure is triggered at a low number of load cycles.

Table 4. Material parameters for the asymmetrically notched test under cyclic loading.

K	ν	w_0	η_d	γ_0	k	n_y	σ_1^p	H_1^{iso}	H_1^{kin}	η_p	β
[MPa]	[-]	[MPa]	[N ^{1/2}]	[MPa]	[-]	[-]	[MPa]	[MPa]	[MPa]	[N ^{1/2}]	[-]
71659.46	0.331	1190.3	2.217	2800	0.4	1	345	0	2500	4	0.4

For the numerical simulations, a finite-element discretization was performed using an unstructured mesh,

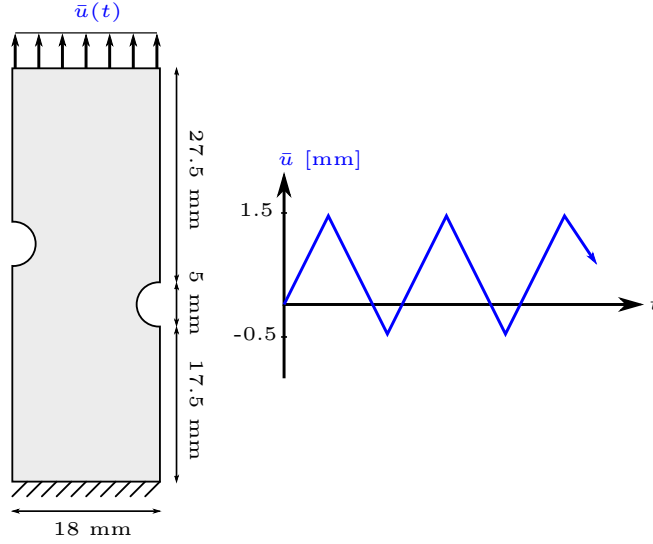


Fig. 12. Schematic representation of the asymmetrically notched specimen under displacement control.

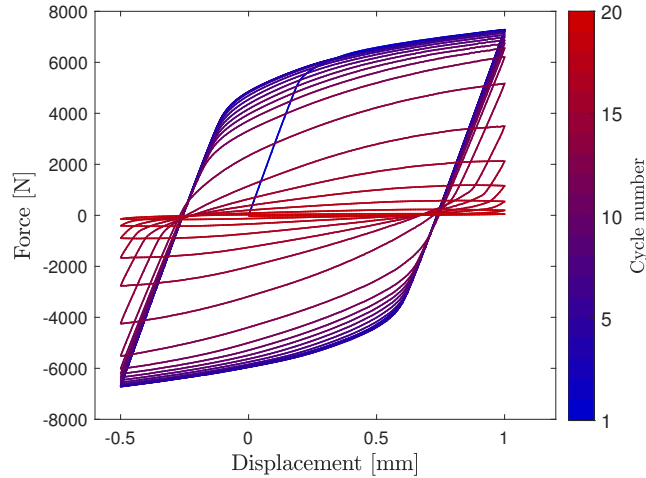


Fig. 13. Force-displacement curve measured at the top border (figure 12) of the asymmetrically notched specimen.

consisting of 9760 bilinear quadrilateral elements. Figure 13 shows the force-displacement response obtained with the parameters shown in table 4. Similar to the homogeneous uniaxial response, we observe an initially stable plastic loop, whose amplitude progressively vanishes as damage evolves.

Figure 14 shows contour plots for the equivalent plastic strains and the phase-field/damage variable at different loading stages. After 6 cycles, the plastic strains are localized in relatively wide bands, governed by the plastic length scale (figure 14a). Within these regions, damage is triggered and begins to evolve (figure 14e). After about 12 cycles, individual cracks initiate and propagate from the notches (figures 14f and 14g), resulting in a strong localization of plastic strains (figures 14b and 14c). At this stage, the diffuse nature of the plastic strains in the pre-cracked states shifts to a strongly localized evolution, thus capturing the behavior of ductile cracks. At subsequent stages, the cracks begin to propagate and finally merge along

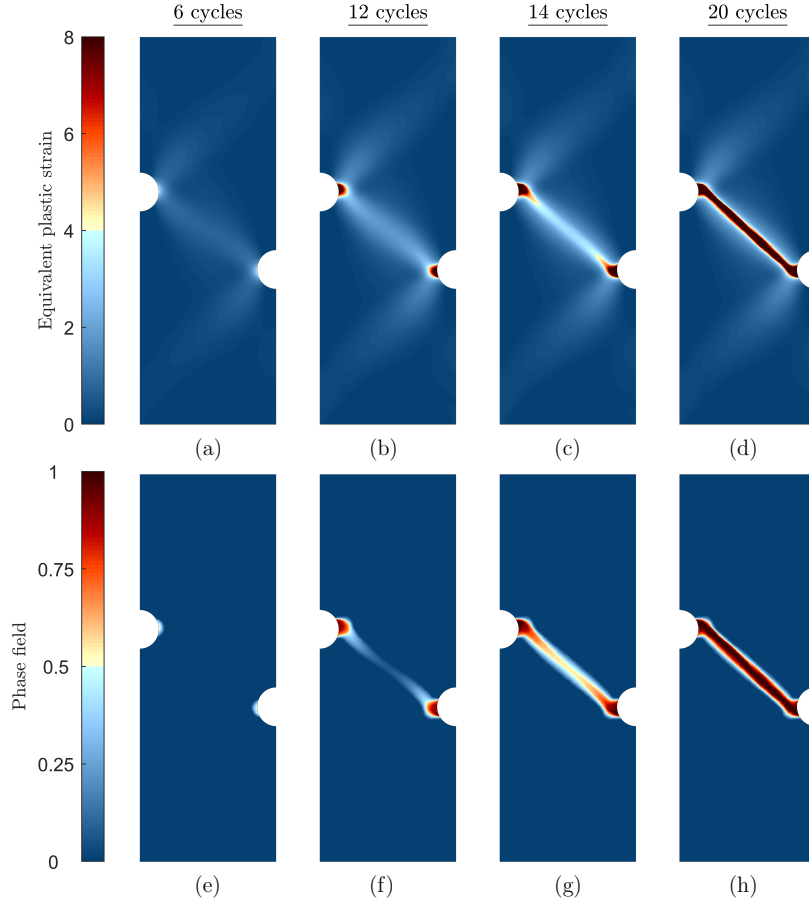


Fig. 14. Equivalent plastic strains (a)-(d) and phase field (e)-(h) during damage initiation (6 cycles), crack initiation (12 cycles), crack propagation (14 cycles) and final merging and rupture stage (20 cycles).

a central shear band, leading to a slip-like failure mode after 20 cycles (figures 14d and 14h).

In the context of the phase-field approach to ductile fracture, similar examples have been studied under monotonic loading [33, 34, 39]. In particular, Rodríguez et al. [39] present different responses that depend on the degree of ductility: a mixed Mode I/II failure associated with an elastoplastic brittle response, and a Mode II-dominated failure associated with a ductile response. In the present study, the cyclic response is strongly driven by plastic strains and therefore resembles the ductile failure mode obtained for monotonic loading by Rodríguez et al. [39].

5. Conclusions

In the context of the energetic formulation, we have presented a coupled gradient-enhanced plasticity-damage model that embeds, in a unified way, characteristic features of low- and high-cycle fatigue. The proposed variational model is able to account for cyclic failure under both force and displacement control by combining a phase-field approach to fatigue cracks with cyclic plasticity, including multi-surface kinematic hardening, isotropic hardening/softening and ratcheting. The multi-field governing equations are derived

from the principles of the energetic formulation, leading to a robust numerical implementation based on an alternate minimization scheme.

The results of numerical simulations indicate that several material responses can be captured by the cyclic plasticity model, including cyclic hardening and cyclic softening effects, as well as ratcheting under force control and stress relaxation under displacement control. Once damage coupling is introduced, the plastic energy accumulation entails a plastic fatigue effect, associated with the low-cycle fatigue regime. The model is further enriched by a fatigue degradation function that is driven by free energy accumulation and degrades the damage resisting force. In the absence of plastic strains, this feature accounts for brittle fracture processes under high-cycle fatigue. The combination of elastic and plastic fatigue mechanisms conceived in an energetic framework allows for a physically sound description of a broad range of fatigue regimes. These results are evidenced in the study of homogeneous uniaxial responses. Moreover, the results of numerical simulations in a 2D setting highlight the ability of the model to describe fatigue-induced ductile fracture, including the initiation, propagation and merging of cohesive cracks.

References

- [1] R.I. Stephens, A. Fatemi, R.R. Stephens, and H.O. Fuchs. *Metal fatigue in engineering*. John Wiley & Sons, 2000.
- [2] J. Lemaitre. *A course on damage mechanics*, volume 2. Springer Berlin, 1996.
- [3] T. Hassan and S. Kyriakides. Ratcheting of cyclically hardening and softening materials: I. uniaxial behavior. *International Journal of Plasticity*, 10(2):149–184, 1994.
- [4] T. Hassan and S. Kyriakides. Ratcheting of cyclically hardening and softening materials: II. multiaxial behavior. *International Journal of Plasticity*, 10(2):185–212, 1994.
- [5] J.L. Chaboche. A review of some plasticity and viscoplasticity constitutive theories. *International Journal of Plasticity*, 24(10):1642–1693, 2008.
- [6] S.K. Paul, S. Sivaprasad, S. Dhar, and S. Tarafder. Cyclic plastic deformation and cyclic hardening/softening behavior in 304ln stainless steel. *Theoretical and Applied Fracture Mechanics*, 54(1):63–70, 2010.
- [7] O.H. Basquin. The exponential law of endurance tests. *Proceedings American Society for Testing Materials*, 10:625–630, 1910.
- [8] P.C. Paris and F. Erdogan. A critical analysis of crack propagation laws. *Journal of Basic Engineering*, 85(4):528–533, 1963.
- [9] R.G. Forman, V.E. Kearney, and R.M. Engle. Numerical analysis of crack propagation in cyclic-loaded structures. *Journal of Basic Engineering*, 89(3):459–463, 1967.
- [10] J. Maierhofer, R. Pippan, and H.P. Gänser. Modified nasgro equation for physically short cracks. *International Journal of Fatigue*, 59:200–207, 2014.
- [11] R. Desmorat. Damage and fatigue: continuum damage mechanics modeling for fatigue of materials and structures. *Revue Européenne de Génie Civil*, 10(6-7):849–877, 2006.
- [12] R. Alessi, S. Vidoli, and L. De Lorenzis. A phenomenological approach to fatigue with a variational phase-field model: The one-dimensional case. *Engineering Fracture Mechanics*, 190:53–73, 2018.
- [13] P. Carrara, M. Ambati, R. Alessi, and L. De Lorenzis. A novel framework to model the fatigue behavior of brittle materials based on a variational phase-field approach. *arXiv preprint arXiv:1811.02244*, 2018.
- [14] G.A. Maugin. Internal variables and dissipative structures. *Journal of Non-Equilibrium Thermodynamics*, 15(2):173–192, 1990.

- [15] C. Miehe. A multi-field incremental variational framework for gradient-extended standard dissipative solids. *Journal of the Mechanics and Physics of Solids*, 59(4):898–923, 2011.
- [16] G. Francfort and J.J. Marigo. Revisiting brittle fracture as an energy minimization problem. *Journal of the Mechanics and Physics of Solids*, 46(8):1319–1342, 1998.
- [17] B. Bourdin, G. Francfort, and J.J. Marigo. Numerical experiments in revisited brittle fracture. *Journal of the Mechanics and Physics of Solids*, 48(4):797–826, 2000.
- [18] B. Bourdin, G. Francfort, and J.J. Marigo. The variational approach to fracture. *Journal of Elasticity*, 91(1-3):5–148, 2008.
- [19] C. Miehe, M. Hofacker, and F. Welschinger. A phase field model for rate-independent crack propagation: Robust algorithmic implementation based on operator splits. *Computer Methods in Applied Mechanics and Engineering*, 199(45):2765–2778, 2010.
- [20] M.J. Borden, C.V. Verhoosel, M.A. Scott, T.J.R. Hughes, and C.M. Landis. A phase-field description of dynamic brittle fracture. *Computer Methods in Applied Mechanics and Engineering*, 217:77–95, 2012.
- [21] M. Ambati, T. Gerasimov, and L. De Lorenzis. A review on phase-field models of brittle fracture and a new fast hybrid formulation. *Computational Mechanics*, 55(2):383–405, 2015.
- [22] K. Pham, H. Amor, J.J. Marigo, and C. Maurini. Gradient damage models and their use to approximate brittle fracture. *International Journal of Damage Mechanics*, 20(4):618–652, 2011.
- [23] K. Pham, J.J. Marigo, and C. Maurini. The issues of the uniqueness and the stability of the homogeneous response in uniaxial tests with gradient damage models. *Journal of the Mechanics and Physics of Solids*, 59(6):1163–1190, 2011.
- [24] J.J. Marigo, C. Maurini, and K. Pham. An overview of the modelling of fracture by gradient damage models. *Meccanica*, 51(12):3107–3128, 2016.
- [25] R. de Borst and C.V. Verhoosel. Gradient damage vs phase-field approaches for fracture: Similarities and differences. *Computer Methods in Applied Mechanics and Engineering*, 312:78–94, 2016.
- [26] N. Moës, J. Dolbow, and T. Belytschko. A finite element method for crack growth without remeshing. *International Journal for Numerical Methods in Engineering*, 46(1):131–150, 1999.
- [27] N. Moës and T. Belytschko. Extended finite element method for cohesive crack growth. *Engineering Fracture Mechanics*, 69(7):813–833, 2002.
- [28] E. Samaniego and T. Belytschko. Continuum–discontinuum modelling of shear bands. *International Journal for Numerical Methods in Engineering*, 62(13):1857–1872, 2005.

- [29] J.Y. Wu, V.P. Nguyen, C.T. Nguyen, D. Sutula, S. Bordas, and S. Sinaie. Phase field modeling of fracture. *Advances in Applied Mechanics: Multi-scale Theory and Computation*, 52, 2018.
- [30] R. Alessi, J.J. Marigo, and S. Vidoli. Gradient damage models coupled with plasticity and nucleation of cohesive cracks. *Archive for Rational Mechanics and Analysis*, 214(2):575–615, 2014.
- [31] R. Alessi, J.J. Marigo, and S. Vidoli. Gradient damage models coupled with plasticity: variational formulation and main properties. *Mechanics of Materials*, 80:351–367, 2015.
- [32] R. Alessi, V. Crismale, and G. Orlando. Fatigue effects in elastic materials with variational damage models: A vanishing viscosity approach. *Journal of Nonlinear Science*, 29(3):1041–1094, 2019.
- [33] F.P. Duda, A. Ciaronetti, P.J. Sánchez, and A.E. Huespe. A phase-field/gradient damage model for brittle fracture in elastic–plastic solids. *International Journal of Plasticity*, 65:269–296, 2015.
- [34] M. Ambati, T. Gerasimov, and L. De Lorenzis. Phase-field modeling of ductile fracture. *Computational Mechanics*, 55(5):1017–1040, 2015.
- [35] M.J. Borden, T.J.R. Hughes, C.M. Landis, A. Anvari, and I.J. Lee. A phase-field formulation for fracture in ductile materials: Finite deformation balance law derivation, plastic degradation, and stress triaxiality effects. *Computer Methods in Applied Mechanics and Engineering*, 312:130–166, 2016.
- [36] C. Kuhn, T. Noll, and R. Müller. On phase field modeling of ductile fracture. *GAMM-Mitteilungen*, 39(1):35–54, 2016.
- [37] C. Miehe, S. Teichtmeister, and F. Aldakheel. Phase-field modelling of ductile fracture: a variational gradient-extended plasticity-damage theory and its micromorphic regularization. *Philosophical Transactions of the Royal Society A: Mathematical, Physical and Engineering Science*, 374(2066):20150170, 2016.
- [38] J. Ulloa, P. Rodríguez, and E. Samaniego. On the modeling of dissipative mechanisms in a ductile softening bar. *Journal of Mechanics of Materials and Structures*, 11(4):463–490, 2016.
- [39] P. Rodríguez, J. Ulloa, C. Samaniego, and E. Samaniego. A variational approach to the phase field modeling of brittle and ductile fracture. *International Journal of Mechanical Sciences*, 144:502–517, 2018.
- [40] J. Fang, C. Wu, J. Li, Q. Liu, C. Wu, G. Sun, and L. Qing. Phase field fracture in elasto-plastic solids: variational formulation for multi-surface plasticity and effects of plastic yield surfaces and hardening. *International Journal of Mechanical Sciences*, 156:382–396, 2019.
- [41] R. Alessi, M. Ambati, T. Gerasimov, S. Vidoli, and L. De Lorenzis. Comparison of phase-field models of fracture coupled with plasticity. In *Advances in Computational Plasticity*, pages 1–21. Springer, 2018.

- [42] A. Mesgarnejad, A. Imanian, and A. Karma. Phase-field models for fatigue crack growth. *arXiv preprint arXiv:1901.00757*, 2018.
- [43] M. Seiler, T. Linse, P. Hantschke, and M. Kästner. An efficient phase-field model for fatigue fracture in ductile materials. *arXiv preprint arXiv:1903.06465*, 2019.
- [44] Y.S. Lo, M.J. Borden, K. Ravi-Chandar, and C.M. Landis. A phase-field model for fatigue crack growth. *Journal of the Mechanics and Physics of Solids*, 132:103684, 2019.
- [45] J.L. Chaboche. Time-independent constitutive theories for cyclic plasticity. *International Journal of Plasticity*, 2(2):149–188, 1986.
- [46] J.L. Chaboche. Constitutive equations for cyclic plasticity and cyclic viscoplasticity. *International Journal of Plasticity*, 5(3):247–302, 1989.
- [47] J.L. Chaboche. On some modifications of kinematic hardening to improve the description of ratchetting effects. *International Journal of Plasticity*, 7(7):661–678, 1991.
- [48] G.T. Houlsby, C.N. Abadie, W.J.A.P. Beuckelaers, and B.W. Byrne. A model for nonlinear hysteretic and ratcheting behaviour. *International Journal of Solids and Structures*, 120:67–80, 2017.
- [49] P.J. Armstrong and C.O. Frederick. A mathematical representation of the multiaxial bauschinger effect. Technical Report RD/B/N 731, Berkeley Nuclear Laboratories, Central Electricity Generating Board, 1966.
- [50] C.O. Frederick and P.J. Armstrong. A mathematical representation of the multiaxial bauschinger effect. *Materials at High Temperatures*, 24(1):1–26, 2007.
- [51] J.J. Moreau. Sur les lois de frottement, de viscosité et de plasticité. *Comptes rendus de l'Académie des Sciences, Paris*, 271:608–611, 1970.
- [52] B. Halphen and Q.S. Nguyen. Generalized standard materials. *Journal de Mécanique*, 14(1):39–63, 1975.
- [53] P. Germain, P. Suquet, and Q.S. Nguyen. Continuum thermodynamics. *Journal of Applied Mechanics*, 50:1010–1020, 1983.
- [54] H. Ziegler and C. Wehrli. The derivation of constitutive relations from the free energy and the dissipation function. In *Advances in Applied Mechanics*, volume 25, pages 183–238. Elsevier, 1987.
- [55] J.C. Simo, J.G. Kennedy, and R.L. Taylor. Complementary mixed finite element formulations for elastoplasticity. *Computer Methods in Applied Mechanics and Engineering*, 74(2):177–206, 1989.
- [56] C. Comi and U. Perego. A unified approach for variationally consistent finite elements in elastoplasticity. *Computer Methods in Applied Mechanics and Engineering*, 121(1-4):323–344, 1995.

- [57] W. Han and B.D. Reddy. *Plasticity: mathematical theory and numerical analysis*, volume 9. Springer Science & Business Media, 1999.
- [58] K. Hackl. Generalized standard media and variational principles in classical and finite strain elastoplasticity. *Journal of the Mechanics and Physics of Solids*, 45(5):667–688, 1997.
- [59] M. Ortiz and L. Stainier. The variational formulation of viscoplastic constitutive updates. *Computer Methods in Applied Mechanics and Engineering*, 171(3-4):419–444, 1999.
- [60] C. Miehe. Strain-driven homogenization of inelastic microstructures and composites based on an incremental variational formulation. *International Journal for Numerical Methods in Engineering*, 55(11):1285–1322, 2002.
- [61] C. Carstensen, K. Hackl, and A. Mielke. Non-convex potentials and microstructures in finite-strain plasticity. In *Proceedings of the Royal Society of London A: Mathematical, Physical and Engineering Sciences*, volume 458, pages 299–317. The Royal Society, 2002.
- [62] C. Comi. Computational modelling of gradient-enhanced damage in quasi-brittle materials. *Mechanics of Cohesive-frictional Materials*, 4(1):17–36, 1999.
- [63] M.E. Gurtin and L. Anand. Thermodynamics applied to gradient theories involving the accumulated plastic strain: the theories of aifantis and fleck and hutchinson and their generalization. *Journal of the Mechanics and Physics of Solids*, 57(3):405–421, 2009.
- [64] N.A. Fleck and J.R. Willis. A mathematical basis for strain-gradient plasticity theory—part I: Scalar plastic multiplier. *Journal of the Mechanics and Physics of Solids*, 57(1):161–177, 2009.
- [65] G.A. Maugin. The method of virtual power in continuum mechanics: Application to coupled fields. *Acta Mechanica*, 35(1-2):1–70, 1980.
- [66] H. Petryk. Incremental energy minimization in dissipative solids. *Comptes Rendus Mecanique*, 331(7):469–474, 2003.
- [67] A. Mielke. A mathematical framework for generalized standard materials in the rate-independent case. *Multifield Problems in Solid and Fluid Mechanics*, 28:399–428, 2006.
- [68] A. Mielke and T. Roubíček. *Rate-Independent systems. Theory and application*. Springer, 2015.
- [69] R. Alessi. Energetic formulation for rate-independent processes: remarks on discontinuous evolutions with a simple example. *Acta Mechanica*, 227(10):2805–2829, 2016.
- [70] G. Lancioni. Modeling the response of tensile steel bars by means of incremental energy minimization. *Journal of Elasticity*, 121(1):25–54, 2015.

- [71] O. Rokoš, J. Zeman, and M. Jirásek. Localization analysis of an energy-based fourth-order gradient plasticity model. *European Journal of Mechanics-A/Solids*, 55:256–277, 2016.
- [72] M. Luege, A. Orlando, M.E. Almenar, and E.A. Pilotta. An energetic formulation of a gradient damage model for concrete and its numerical implementation. *International Journal of Solids and Structures*, 155:160–184, 2018.
- [73] R. Alessi, J.J. Marigo, C. Maurini, and S. Vidoli. Coupling damage and plasticity for a phase-field regularisation of brittle, cohesive and ductile fracture: one-dimensional examples. *International Journal of Mechanical Sciences*, 149:559–576, 2018.
- [74] R. Alessi and D. Bernardini. Analysis of localization phenomena in shape memory alloys bars by a variational approach. *International Journal of Solids and Structures*, 73:113–133, 2015.
- [75] R. Alessi and K. Pham. Variational formulation and stability analysis of a three dimensional superelastic model for shape memory alloys. *Journal of the Mechanics and Physics of Solids*, 87:150–176, 2016.
- [76] J. Mosler and O.T. Bruhns. Towards variational constitutive updates for non-associative plasticity models at finite strain: models based on a volumetric-deviatoric split. *International Journal of Solids and Structures*, 46(7-8):1676–1684, 2009.
- [77] J. Mosler. Variationally consistent modeling of finite strain plasticity theory with non-linear kinematic hardening. *Computer Methods in Applied Mechanics and Engineering*, 199(45-48):2753–2764, 2010.
- [78] G.A. Francfort and U. Stefanelli. Quasi-static evolution for the armstrong–frederick hardening-plasticity model. *Applied Mathematics Research eXpress*, 2013(2):297–344, 2013.
- [79] G.A. Francfort. Recovering convexity in non-associated plasticity. *Comptes Rendus Mécanique*, 346(3):198–205, 2018.
- [80] G.T. Houlsby and A.M. Puzrin. *Principles of hyperplasticity: an approach to plasticity theory based on thermodynamic principles*. Springer Science & Business Media, 2007.
- [81] M.A. Biot. *Mechanics of incremental deformations*. Wiley, 1965.
- [82] C.N. Abadie. *Cyclic lateral loading of monopile foundations in cohesionless soils*. PhD thesis, 2015.
- [83] H.B. Mühlhaus and E.C. Alfantis. A variational principle for gradient plasticity. *International Journal of Solids and Structures*, 28(7):845–857, 1991.
- [84] R. de Borst and H.B. Mühlhaus. Gradient-dependent plasticity: formulation and algorithmic aspects. *International Journal for Numerical Methods in Engineering*, 35:521–539, 1992.
- [85] Q.S. Nguyen. Quasi-static responses and variational principles in gradient plasticity. *Journal of the Mechanics and Physics of Solids*, 97:156–167, 2016.

- [86] G.A. Maugin. *The thermomechanics of plasticity and fracture*, volume 7. Cambridge University Press, 1992.
- [87] J.C. Simo and T.J.R. Hughes. *Computational inelasticity*. Springer, 1998.
- [88] H. Amor, J.J. Marigo, and C. Maurini. Regularized formulation of the variational brittle fracture with unilateral contact: numerical experiments. *Journal of the Mechanics and Physics of Solids*, 57(8): 1209–1229, 2009.
- [89] L. Ambrosio and V.M. Tortorelli. Approximation of functional depending on jumps by elliptic functional via t-convergence. *Communications on Pure and Applied Mathematics*, 43(8):999–1036, 1990.
- [90] B. Bourdin. Numerical implementation of the variational formulation for quasi-static brittle fracture. *Interfaces and Free Boundaries*, 9(3):411–430, 2007.
- [91] T. Gerasimov and L. De Lorenzis. On penalization in variational phase-field models of brittle fracture. *Computer Methods in Applied Mechanics and Engineering*, 354(2):990–1026, 2019.